RESEARCH ARTICLE

VOLCANICA

Multiple sources of elevation change during and after the 2011–2012 Cordón Caulle, Chile eruption measured by satellite topographic time series

Diego Lobos-Lillo *[α], Francisco Delgado[β], Matthew E. Pritchard[α], Philipp P. Ruprecht[γ], and Carolina Muñoz-Saez[γ]

[α] Department of Earth and Atmospheric Sciences, Cornell University, Ithaca, New York, USA.
[β] Departamento de Geología y Centro de Excelencia en Geotermia de los Andes, FCFM, Universidad de Chile, Plaza Ercilla 803, Santiago, Chile.
[γ] Department of Geological Sciences and Engineering, University of Nevada, Reno, USA.

Submitted: 2023-10-27 | Accepted: 2024-05-30 | Published: 2024-07-28

Editor: S K Ebmeier | Typesetter: J Farquharson

Abstract

The 2011–2012 eruption at Cordón Caulle, Chile offers an exceptional opportunity to investigate topographic evolution of a laccolith, lava flows, and tephra during and after rhyolitic eruptions using satellite TanDEM-X and Plèiades data. We find distinct phases: rapid surface uplift from the laccolith and tephra (June–August 2011) and lava (June 2011–March 2012), followed by a reduction in the elevation of the laccolith and tephra (up to 19 m yr^{-1}) until February 2013, and slower subsidence of all deposits until 2019 (the most recent data). The spatial distribution of subsidence-to-uplift ratios shows different volcanic and geomorphological processes occurring (degassing, cooling, crystallization, lateral movement, compaction, erosion). Pre-eruptive river channels showed elevation increases of up to 10–50 m due to tephra deposition, but this tephra was largely removed within three to four years. This research shows the potential of repeating high-resolution remote sensing elevation data to elucidate volcanic landscape evolution and yields insights into the co- and post-eruptive evolution of deposits.

Resumen

La erupción de 2011–2012 en Cordón Caulle, Chile, resultó en la formación de un lacolito, ofreciendo una oportunidad excepcional para investigar la evolución topográfica durante las erupciones riolíticas utilizando TanDEM-X y Plèiades. Un análisis que abarcó desde enero de 2011 hasta noviembre de 2019 identificó fases distintivas: rápido levantamiento durante la fase efusiva de la erupción (enero–agosto de 2011), seguido de una subsidencia acelerada hasta febrero de 2013, y un periodo de estabilidad relativa a partir de entonces. La distribución espacial de las proporciones de subsidencia a elevación destacó las zonas de deposición de tefra y los sistemas fluviales como áreas de considerable transformación geomorfológica. Los canales de los ríos pre-eruptivos mostraron variaciones de profundidad notables de hasta 10–50 metros y en gran medida se restauraron a su estado pre-erupción dentro de tres a cuatro años. Esta investigación aprovecha los datos de sensores remotos de alta resolución para evidenciar la evolución topográfica y ofrece ideas claves sobre la dinámica y los efectos duraderos de las formaciones de lacolitos.

Keywords: Cordon Caulle; Explosive-effusive volcanism; Laccolith; Magma intrusion; Rhyolitic; Tephra deposition.

1 Introduction

Volcanic activity brings about significant topographic changes through a variety of processes, including tephra deposition, lava flow emplacement, and the formation of shallow magma bodies such as laccoliths [e.g. Acocella 2021]. Understanding the relative contributions of these processes is crucial in studying the temporal evolution of volcanic landscapes, as it provides insights into eruption dynamics and post-eruptive surface changes. Laccoliths are characterized by their dome-shaped geometry and ability to cause forced folding of overburden as the magma accumulates underground. Forced folding, as described by Stearns [1978], occurs when the emplacement and growth of a laccolith deforms the overburden, causing the rock layers to fold in a manner that mimics the shape of the intruding magma body. This process is accompanied by seismic activity, ground deformation, and gas emissions, which are indicative of the active magmatic processes occurring at depth [e.g. Corry 1988; Menand 2011; Magee 2024]. Improved understanding of the mechanics of emplacement and post-emplacement changes to shallow magma bodies, particularly laccoliths, could lead to a more accurate eruption forecasting, hazard assessment and mitigation strategies [e.g. Menand 2011; Carlino 2012; Segall 2013; Gudmundsson et al. 2022]. The Cordón Caulle volcano, located in the Southern Andes of Chile, provides a unique case study for investigating shallow magma dynamics and their role in volcanic topographic evolution through the interplay of laccolith formation and eruption deposits in the last decade (Figure 1).

1.1 Geological setting

The Puyehue-Cordón Caulle Volcanic Complex (PCC) (Figure 1) is an active volcanic center situated in the Southern Andes Volcanic Zone, characterized by a diverse eruptive history dating back to the Middle Pleistocene [Lara et al. 2006; Singer et al. 2008], and is compositionally diverse, with a range of volcanic rocks including basaltic andesites, andesites, and

* dal344@cornell.edu

rhyolites [Singer et al. 2008]. Situated at the intersection of the Liquiñe-Ofqui Fault Zone (LOFZ) and an ancient NW-SE basement structure (Figure 1), the complex comprises the Cordillera Nevada caldera, the Cordón Caulle fissure system, and the Puyehue stratovolcano [Lara et al. 2004; Lara et al. 2006; Singer et al. 2008]. While initial activity was distributed across these structures, the Late Pleistocene marked a focus on the Cordón Caulle and Puyehue features, which have since exhibited some of the highest eruptive rates in the Southern Andes—approximately 0.42 $km^3\ yr^{-1}$ [Singer et al. 2008]. The Cordón Caulle system has been the location of three major eruptions in the past century, specifically in 1921–1922, 1960, and 2011–2012 (Figure 1). The 1960 eruption was particularly noteworthy as it was triggered by the 9.5 M_w Valdivia earthquake, the largest recorded subduction-zone earthquake, and occurred 38 hours after the main shock, suggesting a tectonic-volcanic connection [e.g. Barrientos 1994; Lara et al. 2004; Sepúlveda et al. 2005; Lara et al. 2006]. Each of these eruptions was characterized by dacitic to rhyolitic compositions [Singer et al. 2008; Castro et al. 2013], suggesting a shared deep magmatic source [Sepúlveda et al. 2005; Singer et al. 2008; Jay et al. 2014; Delgado 2021; Seropian et al. 2021; Winslow et al. 2022; Phelps et al. 2023].

1.2 Cordón Caulle 2011–2012 eruption

The 9-month long eruption of the Cordón Caulle volcano during 2011–2012, is regarded as one of the 21st century's most impactful volcanic events [e.g. Craig et al. 2016a; b; Elissondo et al. 2016; Dominguez et al. 2020; 2021; Vergara-Pinto and Romero 2023]. It expelled roughly ~0.4 km^3 dense rock equivalent (DRE) of rhyolite tephra [Pistolesi et al. 2015; Naranjo et al. 2017] and led to the formation of a ~0.8 km^3 DRE laccolith [Castro et al. 2016], accompanied by a lava flow measuring ~0.6 km^3 DRE [Castro et al. 2016; Delgado et al. 2019; Delgado 2021]. The extent of the laccolith and the lava flow are shown in Figure 2. This figure also shows the tephra isopachs from the 2011 eruption [Bertrand et al. 2014], highlighting the widespread impact of the tephra fallout. The contours in Figure 2 represent the height differences (dH) between the January 2011 and April 2014 DEMs, showcasing the topographic changes caused by the eruption. However, there has been a significant challenge in rigorously differentiating the volume of the lava flow from that of the laccolith, primarily because the lava flow rests atop the area deformed by the laccolith. The total volume of magma drained from the main Cordón Caulle magma reservoir that is linked to the km-scale deformation throughout the Cordón Caulle fissure system was about ~1.8 km^3 DRE [Delgado 2021]. This reservoir fed the laccolith, tephra eruption, and lava flow and has been potentially reestablished [Phelps et al. 2023]. Studies by Jay et al. [2014], Castro et al. [2016], Seropian et al. [2021], Winslow et al. [2022], and Phelps et al. [2023] indicate that prior to ascending to form the shallow laccolith, the magma was stored in a main reservoir at depths ranging from 2.5 to 10 km, within temperature conditions of 870 to 910 °C. Infrequent mafic enclaves detected in the erupted materials imply that the erupted crystal-poor rhyolite was fuelled by a basaltic mush with a small amount of direct mafic recharge [Winslow et al. 2022]. These basaltic magmas carried an increased supply of melt, volatile elements, and heat from deeper sources, which likely contributed to the creation of an eruptible magma body in the mid-upper crust [Winslow et al. 2022].

The eruption sequence of the Cordón Caulle volcano started with a sub-plinian explosive phase on June 4, 2011, following two months of precursor volcano-seismic activity [Basualto et al. 2023]. The eruption persisted for nine months, finishing on March 2012, impacting a vast region of southern Chile and Argentina with ash and gas emissions [Castro et al. 2013; Wilson et al. 2013; Elissondo et al. 2016; Vergara-Pinto and Romero 2023]. The apex of the explosive episode generated eruptive columns soaring up to 14 km above the vent and mass flow rates reaching approximately ~ $10^7\ kg\,s^{-1}$ [Bonadonna et al. 2015]. The eruption exhibited a combination of explosive and effusive phases, resulting in the creation of a new volcanic cone along with substantial emissions of ash and lava [Lara et al. 2004; Castro et al. 2016; Delgado 2021; Seropian et al. 2021; Crozier et al. 2022]. Moreover, the eruption is associated with the formation of a ~200 m deep magma body, interpreted as a laccolith [Castro et al. 2016], between June 8 and July 3, 2011, with a magma flux reaching up to 150 $m^3\,s^{-1}$ (~ $10^6\ kg\,s^{-1}$) [Castro et al. 2016; Delgado et al. 2019; Delgado 2021].

The eruption subsequently entered a hybrid phase, marked by the extrusion of mostly outgassed rhyolite lava starting on June 15, 2011, exhibiting an extrusion rate of 40 $m^3\,s^{-1}$ [Bertin et al. 2015; Coppola et al. 2017; Delgado et al. 2019]. This lava extrusion persisted for nine months at an average rate of 17 $m^3\,s^{-1}$ [Schipper et al. 2013]. This phase was coupled with the passive outgassing of the lava flow and robust, sustained gas and tephra venting of variable intensity [Crozier et al. 2022]. This behavior typically coincided with mild explosive activity including semi-continuous tephra jetting, ejection of ballistic materials, and Vulcanian-like blasts [Schipper et al. 2013]. During this phase, eruptive columns remained less than 6 km high with an ejection mass rate considerably less than $10^6\ kg\,s^{-1}$ [Bonadonna et al. 2015]. Despite the cessation of magma supply in late March 2012, extruded lava continued to flow until at least January 2013 more likely due to post-emplacement processes [Schipper et al. 2013].

1.3 Cordón Caulle laccolith

One of the most intriguing phenomena associated with the Cordón Caulle 2011–2012 eruption was the rapid lateral emplacement of a laccolith only 20-200 m beneath the surface. It is interpreted as a shallow, relatively flat-lying magma body [Castro et al. 2016; Delgado 2021]. We use the term laccolith, recognizing that dome or cryptodome may also be appropriate descriptions. This laccolith was unique in that it formed during the eruption rather than before or after, challenging the long-held view that intrusions must precede and feed eruptions [Castro et al. 2016]. The results of the models of deformation and conduit flow indicate depths of the laccoliths of only 20–200 m and overpressures of 1–10 MPa that caused surface uplift of 250 m in a few months as shown in Figure 2 [Castro et al. 2016; Delgado et al. 2019; Delgado 2021]. The growth and deformation associated with the laccolith provide valuable insights into the dynamics of magma ascent and in-

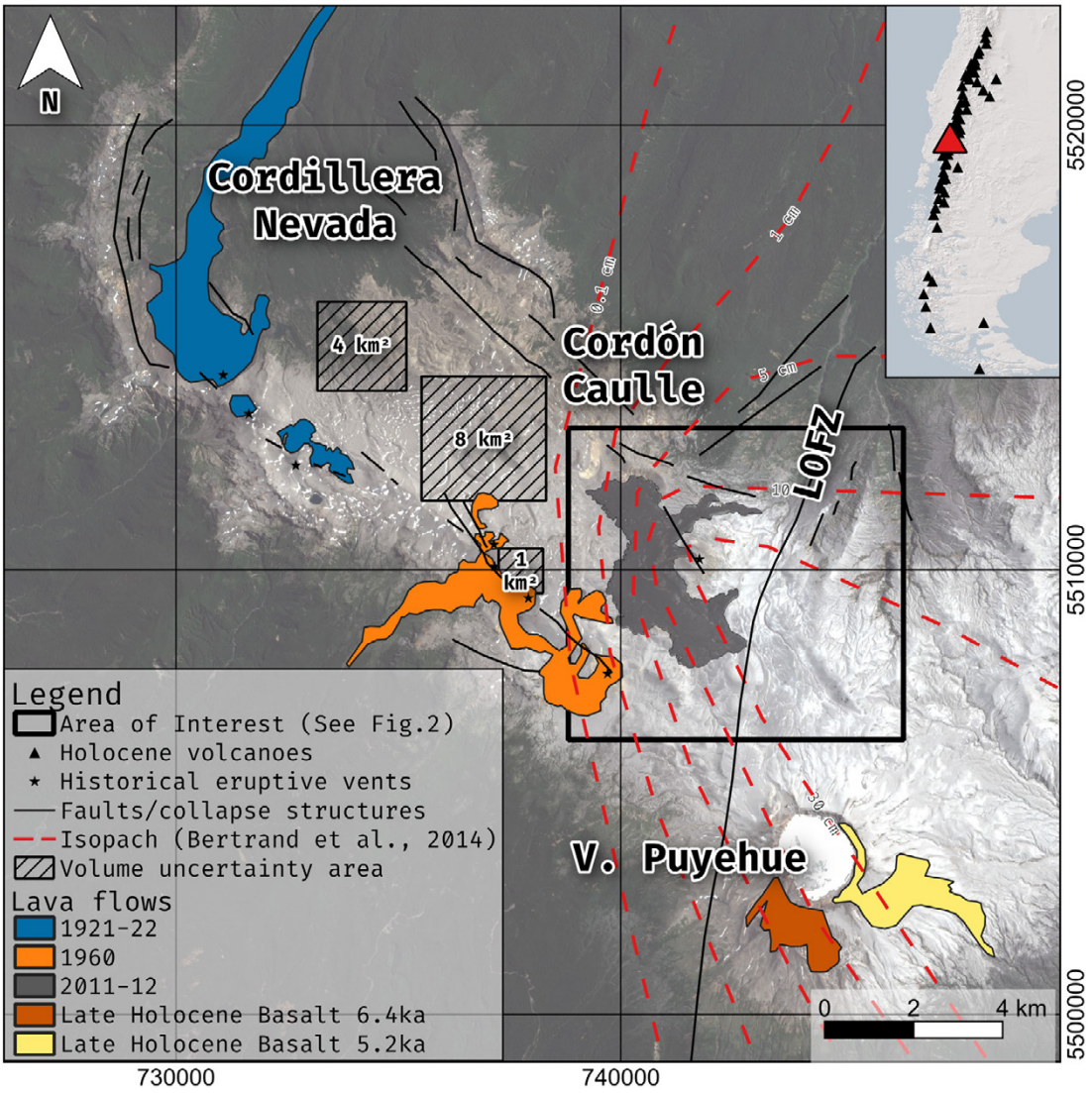

Figure 1: Map of the Puyehue–Cordón Caulle volcanic complex showing lava flows from past eruptions, eruptive vents, 2011 tephra isopachs, and fault structures [Sepúlveda et al. 2004; Singer et al. 2008; Bertrand et al. 2014; Jay et al. 2014]. Dark dashed rectangles denote areas used for volume uncertainty calculations (See Section *2.2.3*), and the solid rectangle highlights the subset area shown in Figure 2 and Figure 3 The inset illustrates the Andean Southern Volcanic Zone with Holocene volcanoes marked by black triangles, as per the Global Volcanism Program [2023], and the red triangle indicating Cordón Caulle.

trusion at Cordón Caulle, and it has been studied with remote sensing [Schipper et al. 2013; Jay et al. 2014; Castro et al. 2016; Euillades et al. 2017; Wendt et al. 2017; Delgado et al. 2018; 2019; Delgado 2021; Schipper et al. 2021; Seropian et al. 2021]. Syn-eruptive laccolith formation is a phenomenon rarely observed, with only a handful of well-documented examples. These include:

The 1943–1945 eruption of Usu volcano in Hokkaido, Japan, which led to the formation of the Showa-Shinzan lava dome due to a laccolith intrusion [Minakami et al. 1951; Yokoyama and Seino 2000; Yokoyama 2002; 2004].

The 1980 eruption of Mt. St Helens in the USA. Prior to the cataclysmic eruption, a cryptodome, led to significant deformations in the north flank of the volcano [Lipman et al. 1981].

The Nishiyama-Shinzan cryptodome formation during the 2000 eruption of Usu volcano in Japan. This event exhibited a sequence of ground uplifts and minor eruptions [Ui et al. 2002; Yamagishi et al. 2004; Saba et al. 2007; Sakagami, M. et al. 2010].

Like the Cordón Caulle event, the 1943–1945 eruption of Usu and the 1980 eruption of Mt. St. Helens offer invaluable insights into the intricate interplay between magmatic intrusions and volcanic eruptions. The 1943–1945 eruption of Usu volcano in Japan was characterized by the emplacement of a lava dome and cryptodome, which caused significant ground deformation and forced folding of the overburden [Minakami et al. 1951; Yokoyama and Seino 2000; Yokoyama 2002; 2004]. The cryptodome intrusion ultimately led to a summit eruption and the formation of a new lava dome. Similarly, the

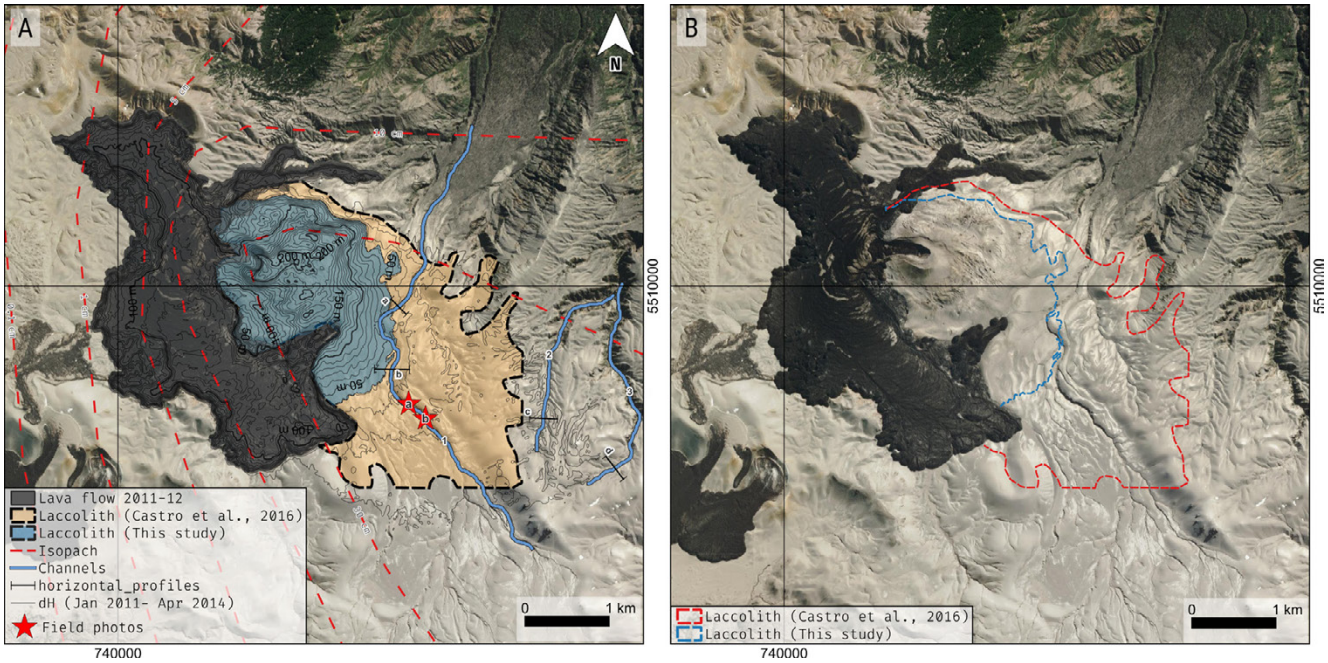

Figure 2: [A] Interpreted map of the Puyehue–Cordón Caulle 2011–2012 eruption site. The dark shading illustrates the final lava outline, while the laccolith extent from Castro et al. [2016] and this study are shown in orange and blue, respectively. Red isopachs of the 2011 tephra are from [Bertrand et al. 2014]. Locations for photos in Figure 16 are marked with red stars. Contours indicate height differences (dH) between the January 2011 and April 2014 DEMs. Black lines labeled a-d delineate horizontal profiles over the channels (Figure 15), while blue lines indicate the channels themselves (longitudinal profiles found in Figure 13) [B] Uninterpreted map of the Puyehue–Cordón Caulle region, showing the topography and location of the 2011–2012 eruption site.

1980 eruption of Mt. St. Helens in the United States was preceded by the intrusion of a cryptodome, which caused severe bulging of the volcano north flank. The cryptodome growth and subsequent collapse triggered a catastrophic lateral blast, highlighting the hazards associated with shallow magma intrusions [Lipman et al. 1981]. These cases demonstrate how magmatic intrusions can deform the host rock, influence the style of eruption, and pose significant risks to surrounding areas. The uniqueness of these events emphasizes the importance of studying the Cordón Caulle eruption and the formation of its associated laccolith to understand better the mechanisms governing laccolith formation and eruption behavior. So far, there are estimates of the laccolith extent (Figure 2), depth, and volume proposed by Castro et al. [2016] and Delgado et al. [2019] who used Digital Elevation Model (DEM) differences and coregistered amplitude images of ENVISAT and TerraSAR-X (TSX). Castro et al. [2016] suggest that the laccolith is 20–200 m deep, it has a volume of 0.8 km^3, an area of 8.2 km^2, and the measured uplift is not significantly influenced by the deposition of tephra. Here we use a more extensive DEM time-series spanning 2011–2019 to explore the multiple sources of elevation change including laccolith formation, post-emplacement evolution, lava flow extrusion and subsidence, and tehpra deposition and erosion.

1.4 Bistatic Interferometric Synthetic Aperture Radar (InSAR)

InSAR has become an indispensable tool for studying volcanic deformation due to its cloud-penetrating capabilities and potential global coverage, making satellite radar ideal for capturing topographic changes over active volcanoes [Burgmann et al. 2000]. As a result, InSAR can provide information about large-scale and long-term deformation of volcanoes, which is unattainable with ground-based equipment [Poland and Zebker 2022]. A range of SAR satellite missions with differing wavelengths and temporal repeat intervals, such as European Space Agency's Sentinel-1 A and B [Torres et al. 2012], the German Aerospace Center's TerraSAR-X (TSX) [Krieger et al. 2007], Japense Aerospace Exploration Agency's Advanced Land Observing Satellite (ALOS) -2 [Rosenqvist et al. 2007], Italian Space Agency's Constellation of small Satellites for the Mediterranean basin Observation (COSMO-SkyMed) [Covello et al. 2010], and Canadian Space Agency's RADARSAT Constellation Mission [Livingstone et al. 2006], contribute to the growing body of SAR data.

To better understand the mechanisms governing laccolith formation and post-eruptive behavior, we employ bistatic InSAR in this study. Unlike multi-pass InSAR, which uses a single satellite radar antenna from multiple flyovers to acquire both reference and repeat images, bistatic InSAR uses single-pass simultaneous observations from two antennas (on one or more spacecraft). This offers the advantage of measuring topography without the atmospheric conditions changing between overflights [Kubanek 2017; Kubanek et al. 2021]. Bistatic InSAR provides some of the highest resolution and most accurate time-lapse topographic change data available, making it invaluable for analyzing ground deformation in volcanic set-

tings, especially in contexts where single-pass InSAR is non-coherent [Kubanek et al. 2021].

The TerraSAR-X add-on for Digital Elevation Measurements (TanDEM-X, or TDX) satellite mission, launched in June 2010, represents a significant advance in global topography quantification [Krieger et al. 2007], which can generate a DEM with a relative 2 m height accuracy [Bachmann et al. 2012; Martone et al. 2012; Rizzoli et al. 2017]. Single-pass InSAR data is crucial in obtaining reliable topographic information, particularly in rapidly changing environments such as volcanoes. The TDX mission employs two satellites, TDX and TSX, that fly in close tandem, capturing synchronized radar images. These images are used to create a bistatic interferogram [Kubanek et al. 2021]. Equipped with advanced X-band SAR sensors, these satellites are responsible for both the transmission and reception of radar signals, which are then transformed into SAR images, provided as coregistered single-look slant range complex (CoSSC) files. The two bistatic SAR images are acquired using a single-pass acquisition geometry, and the phase information from both acquisitions is employed to calculate the interferometric phase [Kubanek 2017; Kubanek et al. 2021; Grémion et al. 2023], which enables the generation of DEMs.

DEMs resulting from bistatic interferograms using TanDEM-X have been employed in various applications, including volcano monitoring and research, due to their high precision and adaptability in data acquisition over rugged terrain or inaccessible regions [Kubanek et al. 2021; Grémion et al. 2023]. For instance, the TanDEM-X mission was used to calculate the height of a lava dome in Montserrat's Soufrière Hills [Wadge et al. 2011] and Merapi volcano in Java, Indonesia [Grémion et al. 2023]; to measure ground deformation associated with volcanic activity at Piton de la Fournaise volcano on Réunion Island [Bato et al. 2016], and Nyamulagira volcano in the Democratic Republic of Congo [Albino et al. 2015]. The mission has also been used to track lava flows on the East Rift Zone of Kīlauea Volcano, Hawai'i [Poland 2014], among other examples.

2 Data and Methods

We create a time series of DEMs for analyzing ground deformation dynamics in the studied volcanic area. We use three types of DEMS: 1) TanDEM-X coregistered single-look slant range complex (CoSSC) data from 2011–2012 used to generate DEMs, henceforth designated as "Reference TDX DEMs" created by Delgado et al. [2019], 2) a Plèiades stereo-optical DEM, also created by Delgado et al. [2019], and 3) CoSSCs from 2012–2019 that we convert to topographic information in this study, hereafter called "CoSSC DEMs". The DEM time series spans from January 27, 2011 to November 28, 2019, providing a more comprehensive understanding than previously available of the laccolith syn- and post-eruptive evolution, its implications, and the role of tephra in the elevation change.

This section outlines our methodology, which is divided into three subsections: first, we describe the TanDEM-X CoSSC and Plèiades DEM data; second, we detail the processing of bistatic interferograms, the estimation of TDX DEM and topographic changes using TanDEM-X data; finally, we discuss the time-series analysis performed on the generated DEM data.

2.1 TanDEM-X CoSSC and Plèiades DEM: reference DEMs

Our study employs the six Reference TDX DEMs from Delgado et al. [2019] (marked with a star in the first column in Table 1), as well as one Plèiades DEM from April 4, 2014 [Castro et al. 2016; Delgado et al. 2019] to compute new bistatic interferograms and ultimately the new TDX DEMs. The CoSSC DEMs were processed using the Delft Object-oriented Radar Interferometric Software (`DORIS`) by Delgado et al. [2019] (see their methods for details on the process). This process yields a high-resolution DEM with a pixel size of 6.6 m (Figure 3). As for the Plèiades optical DEMs, stereo images were acquired on April, 2014, and a DEM was computed using the Institut Geographique National (IGN) `MicMac` photogrammetric software [Delgado et al. 2019]. The resulting high-resolution DEM has a pixel size of 0.5 m resampled to 2 m, providing detailed topographic information for our analysis.

To account for the differences between the CoSSC DEMs and Plèiades DEM, we coregister all the DEMs to the Shuttle Radar Topography Mission DEM [Farr et al. 2007]. We employed the co-registration approach described by Nuth and Kääb [2011], which utilizes an iterative co-registration method named Enhanced Co-registration and Bias Correction (ECBC). This algorithm is designed to reduce errors and biases caused by misregistration between DEMs acquired at different times, resolutions, or from different sources. It is particularly well-suited for applications involving the comparison of DEMs, such as glacier and landslide monitoring or, in our case, analyzing ground deformation in volcanic areas.

First, we masked out the area affected by the eruption based on the Plèiades DEM and the study by Castro et al. [2016]. Following this, we applied the ECBC method [Nuth and Kääb 2011] to accurately coregister the six CoSSC DEMs and Plèiades DEM to the SRTM DEM. The ECBC method involves an iterative process that includes the following steps: 1. Estimating horizontal and vertical offsets between the two DEMs. 2. Calculating elevation differences after correcting for the estimated offsets. 3. Determining the most likely stable areas (i.e. unaffected by the laccolith emplacement and lava effusion). The process is repeated until the offsets converge to stable values. Once the convergence is achieved, the final horizontal and vertical offsets are applied to bring the DEMs into alignment. The effectiveness of this approach is demonstrated in Figure 4, where the black line represents the initial distribution of height differences between the CoSSC DEM and SRTM DEM, and the red line indicates the final distribution. The refinement went from a mean elevation difference of −23.4 m to −2.6 m and a root mean square error (RMSE) of 27.4 m to 16.1 m, indicating an improvement of 85 % in the mean elevation difference and a 41 % reduction in the RMSE calculation.

2.1.1 *Bistatic interferogram processing and topographic change estimation*

The calculation of bistatic interferograms involves several complex steps, including estimating the baseline between the

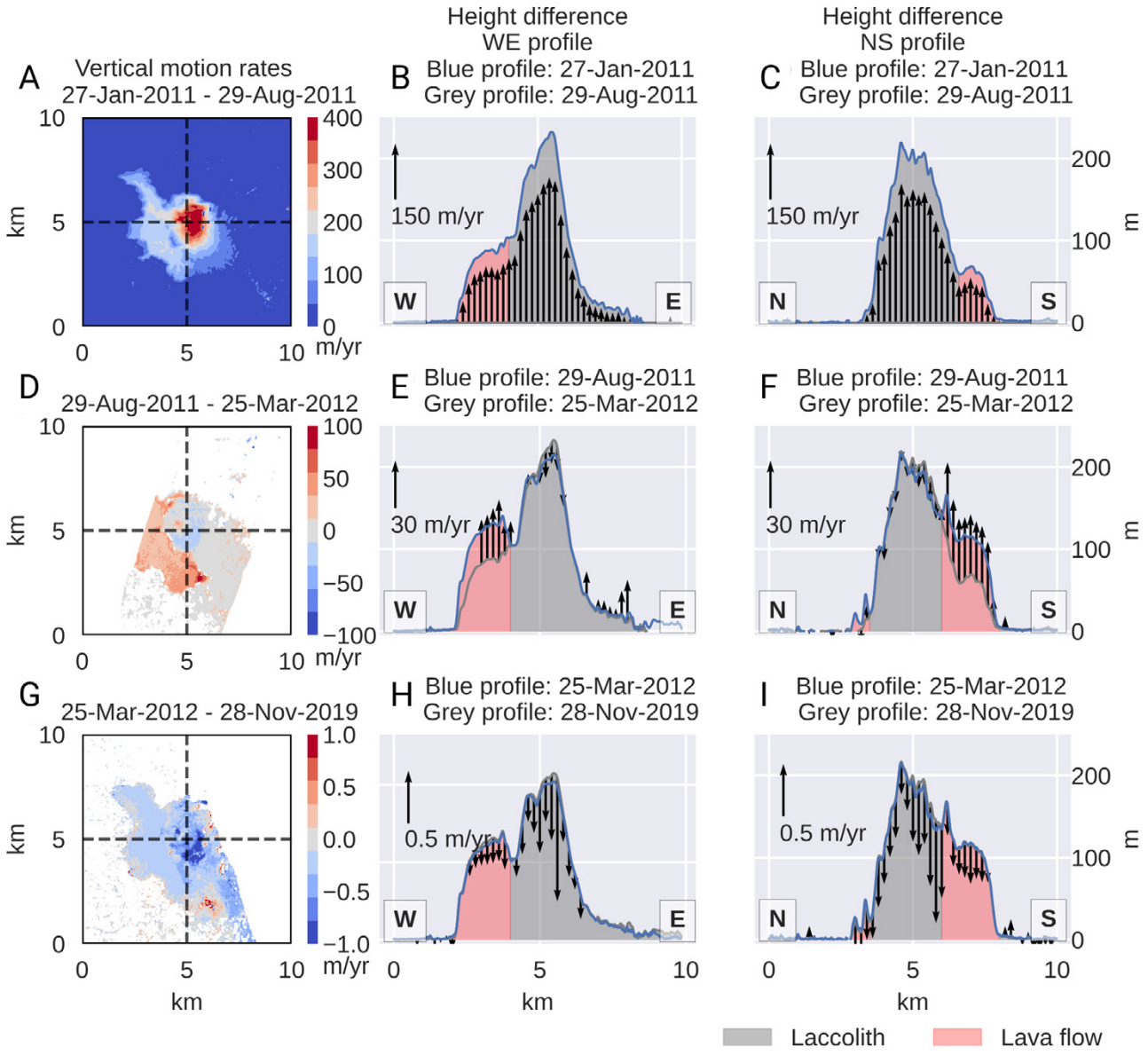

Figure 3: Tracing the velocity (m yr^{-1}) and elevation changes over time at PCC (location in Figure 1), derived from elevation differences from DEM time-series data from TDX, complemented by CoSSC and Plèiades DEMs from Castro et al. [2016] and Delgado et al. [2019]. As seen in Figure 9, three distinct periods (A, D, G) were extracted for detailed analysis. The first row illustrates the laccolith and lava flow emplacement and fast topographic alterations from January 27, 2011 to August 29, 2011. The second row documents a period of accelerated subsidence rates and localized lava flow growth (August 9, 2011 to February 13, 2013), while the third row is a phase of lower subsidence rates (February 13, 2013 to November 28, 2019). The respective West-East and North-South topographic profiles show the initial and final elevations for each time period (B, C, E, F, H, I). The magnitude and direction of arrows correspond to vertical ground uplift or ground subsidence rates from the linear fit on the differential height (dH, Figure 10). Lava and laccolith regions are color-coded within the profiles (red and gray, respectively).

transmitter and receiver antennas, correcting topographic effects, and generating interferometric pairs from multiple acquisitions. These steps are described in detail in several scientific papers [e.g. Poland 2014; Kubanek 2017; Kubanek et al. 2021; Grémion et al. 2023].

To compute the bistatic interferograms, we utilized a modified module for the `stripmapApp` processor of the InSAR Scientific Computing Environment-2 [Rosen et al. 2012] to process bistatic interferograms from CoSSC data. First, the raw SAR data must be pre-processed to correct for various effects, such as range migration and Doppler centroid estimation errors. This can be done using standard SAR processing techniques (e.g. Range-Doppler algorithm) [Bamler and Hartl 1998]. Next, the two SAR images must be co-registered to ensure they are aligned correctly. This is done using several techniques, including cross-correlation and phase correlation [Rosen et al.

2012]. Once the two images are co-registered, an interferogram is generated by calculating the phase difference between them through the hermitian product. Next, the DEM is projected onto range-Doppler coordinates to calculate the simulated topography, and the estimated topographic phase is then removed from the interferogram. We reduce noise by applying the adaptive Goldstein and Werner filter [Goldstein and Werner 1998]. Following the interferogram computation, phase unwrapping is applied to resolve the 2π ambiguity in the phase measurements, utilizing the SNAPHU MCF (Statistical Network Approach to Phase Unwrapping Minimum Cost Flow) algorithm [Chen and Zebker 2000]. The unwrapped interferometric phase (ϕ_{unw}) is converted to terrain height (h) using Equation 1. In this equation, R represents the slant range distance, $B_\perp$ signifies the perpendicular baseline—which is defined as the theoretical distance between the satellites at the time of recording, measured perpendicularly to the look direction—and θ denotes the incidence angle. It is important to note that Equation 1 is an approximation, valid only for 2-D planar orbits, and is based on the parallel ray approximation [Hanssen 2001]:

$$h = -\frac{\lambda R \sin\theta}{2\pi B_\perp}\phi_{unw}. \quad (1)$$

To create a DEM from the converted terrain height, we employed a coherence-based filter with a threshold of 0.65. This filter was designed to mitigate noise and eliminate any unwanted signals, and it was chosen based on Figure 5. Subsequently, the data is geocoded to convert from radar to geographic coordinates. The final step entailed adding the original DEM to the terrain height from Equation 1, assuming that the observed height difference equates to the difference between the original DEM and the interferometric phase ϕ_{bi}.

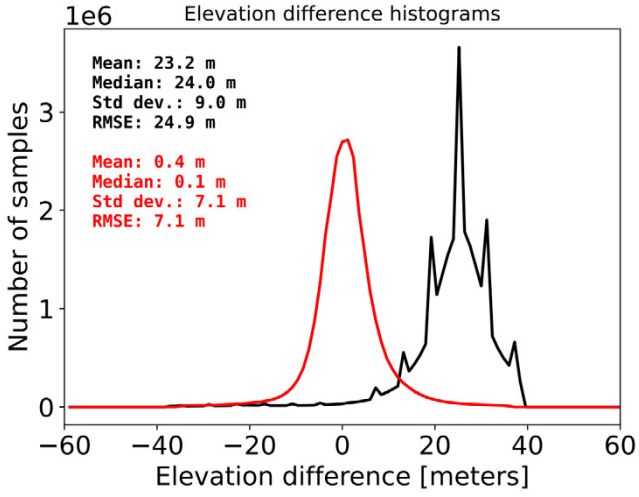

Figure 4: Reduced elevation differences between a subset of the coregistered CoSSC DEM from August 8, 2011, and the SRTM DEM, after masking out areas affected by the eruption based on the Plèiades DEM and the study by Castro et al. [2016]. The black line represents the initial distribution of height differences, while the red line indicates the final distribution after applying the ECBC method.

In the context of single-pass interferometry, we work under the assumption that the interferometric phase is defined as follows:

$$\phi_{bi} = \phi_{ref} + \phi_{topo} + \phi_{noise} + \phi_{orb}. \quad (2)$$

The component ϕ_{orb} corresponds to the effective baseline between acquisitions, approximating half the length of the perpendicular baseline in bistatic mode. In contemporary SAR missions such as those involving the TerraSAR-X and TanDEM-X satellites, the accuracy of satellite orbit determination often surpasses 10 cm for precise science orbits [Yoon

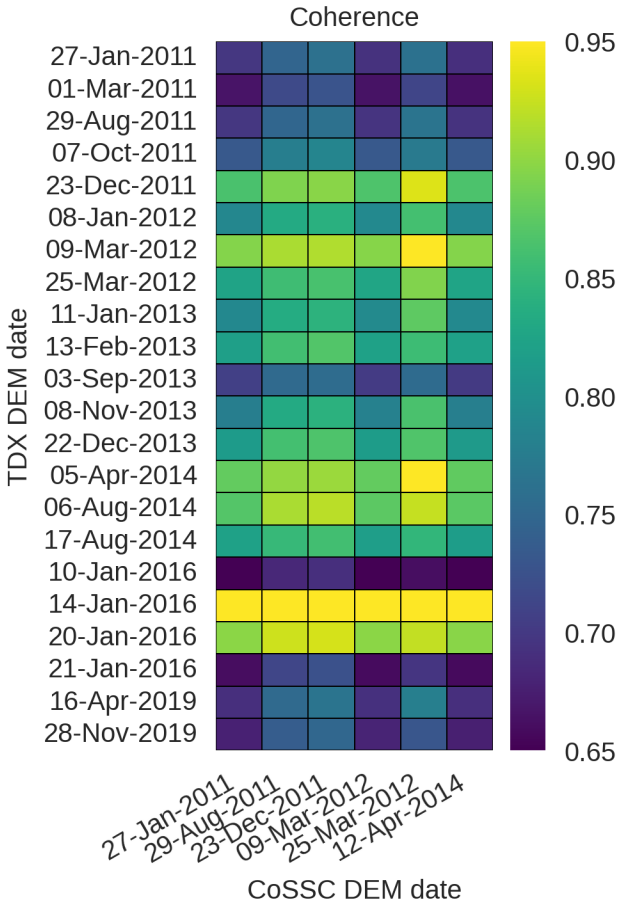

Figure 5: This coherence heatmap of DEM pairs, generated on different dates, is key in understanding the reliability of topographic changes derived from these pairs. Each box represents the coherence value between a reference DEM and a TDX DEM, as identified on the axes. Lighter shades indicate higher coherence values, representing a greater degree of correlation or similarity between the DEM pairs. This visualization emphasizes the variability in DEM coherence, contingent on the chosen reference DEM, underscoring the importance of meticulous DEM pair selection for accurate and reliable topographic analysis. The mean coherence for the entire dataset is 0.8, with a standard deviation of 0.09, indicating a general consistency in the DEM pairs. An explanation of RMSE and NMAD, key parameters in understanding the variations and precision of the DEMs, can be found in Section 2.

et al. 2009; Kubanek et al. 2021]. Consequently, any errors in ϕ_{orb} are deemed negligible. The term ϕ_{ref} denotes the phase attributable to the reference surface, which is eliminated from the DEM, while ϕ_{topo} signifies the change in topographic phase that is the measurement goal.

Our processing led to high-resolution DEMs with a pixel size of 6.6 m (see Figure 3). These DEMs possess an average height accuracy of 0.6 m and an associated vertical error ranging from ±1.8 m to ±4.3 m (detailed in Section 2.2). In this context, "height accuracy" specifically denotes the error in elevation measurements, determined via Equation 6. This calculation considers factors such as the slant range, off-nadir angle, perpendicular baseline, and wavelength (detailed in Section 2.2). This is distinct from "vertical error," a more encompassing term we use to represent the reliability of the DEM's elevation values. This latter metric was derived using statistical methods by comparing each DEM to reference DEMs using the Normalized Median Absolute Deviation (NMAD) and Root Mean Square Error (RMSE) (further discussed in Section 2.2).

2.2 Error analysis

2.2.1 *Statistical error metrics*

In our analysis of the TDX DEM, we consider multiple appropriate error metrics for the elevations. To perform the calculations, we first masked out the water bodies and the areas affected by the 2011–2012 eruption, specifically the lava flows, laccolith, and zones with tephra deposition, as delineated in Castro et al. [2016] and Delgado [2021]. Then, we utilized two commonly employed metrics for comparison between the CoSSC DEMs and the reference TDX and Plèiades DEMs. The first of these metrics is the Root Mean Squared Error (RMSE), as outlined in Equation 3. In this equation, y_i represents the predicted values, x_i stands for the observed values, and n denotes the number of observations. The second metric we used is the Normalized Median Absolute Deviation (NMAD), as detailed in Equation 4. Here, x_i refers to the difference between the two DEMs, while median(x) signifies the median of these differences. The constant scale factor of 1.4826 is an empirically derived value used to normalize the result, thereby rendering it comparable to the standard deviation of a normally distributed dataset.

$$\mathrm{RMSE} = \sqrt{\frac{1}{n}\sum_{i=1}^{n}(y_i - x_i)^2}. \tag{3}$$

In geospatial data contexts, such as with DEMs, RMSE frequently measures the vertical accuracy and overall data quality [Fisher and Tate 2006]. By juxtaposing elevation values from a DEM with a set of recognized reference elevation values, the RMSE can be computed to evaluate the model's reliability and precision. Simultaneously, we also employed the Normalized Median Absolute Deviation (NMAD) because this measure is intimately tied to the median of the absolute variations between the errors and the median error. NMAD serves as a robust estimate for the standard deviation, showing heightened resilience to potential outliers in the dataset [Höhle and Höhle 2009]:

$$\mathrm{NMAD} = 1.4826 \times \mathrm{median}(|x_i - \mathrm{median}(x)|). \tag{4}$$

The RMSE and NMAD results, computed from the comparison between the "new CoSSC DEMs" and the reference DEMs (TDX and Plèiades), are depicted in Figure 6. As the data contains numerous outliers related to the nature of the satellite data, such as speckle error, layover, unwrapping errors, foreshortening, and shadow effects (further explored in Section 2.2.2), the NMAD offers a superior error estimation for the TDX DEM in this instance. The DEMs with the minimum values of RMSE and NMAD are denoted with a star. To construct a DEM time series, we exclusively employed the TDX DEMs presenting the least error. These were visually assessed to confirm data quality prior to their selection for the final TDX DEM time series. In summary, with an average NMAD error of 1.8 m and an average RMSE error of 4.3 m, these values likely bound the vertical uncertainties in our DEMs.

2.2.2 *Satellite based error metrics*

An additional DEM quality metric we utilized is the height of ambiguity (h_{amb}) (see fifth column in Table 1) [Hanssen 2001]. This metric is calculated using Equation 5, where λ is the radar wavelength, R is the range distance, θ is the radar incidence angle, and $B_\perp$ is the perpendicular baseline. This metric quantifies the uncertainty of the height information derived from the phase of the interferometric signal. It is inversely proportional to the interferometric baseline, and thus, larger baselines tend to have lower h_{amb} values, meaning a higher vertical resolution. However, it is also important to note that a smaller h_{amb} is not always better. With a smaller h_{amb}, the sensitivity to height errors increases, potentially leading to phase unwrapping errors, especially in areas with complex topography. Additionally, a larger baseline may cause a decrease in data coherence due to baseline decorrelation [Martone et al. 2012], which in turn can lead to noisier DEMs. Therefore, an optimal balance between a smaller h_{amb} and a sufficient coherence (Figure 5) is often necessary.

$$h_{amb} = \frac{\lambda R \sin\theta}{B_\perp}. \tag{5}$$

From the height ambiguity is also derived the relative height accuracy [Hanssen 2001] for the InSAR DEM and it can be derived as:

$$\sigma_h = \frac{\lambda}{4\pi}\frac{R\sin\theta}{B_\perp}\sigma_\phi = \frac{h_{amb}\sigma_\phi}{4\pi}. \tag{6}$$

Here, σ_ϕ denotes the standard deviation tied to the InSAR phase estimation and is formulated as:

$$\sigma_\phi = \frac{1}{2N_L}\frac{1-\gamma^2}{\gamma^2}. \tag{7}$$

Within this expression, N_L is the count of independent looks, while γ stands for the interferometric coherence as described by [Hanssen 2001]. Given an average coherence, $\gamma = 0.8$, across the computed interferograms, the relative height accuracy σ_h ranges roughly from 0.2 m to 1.9 m, based on varying

perpendicular baseline distances (refer to Table 1), so, the average value for height accuracy is 0.6 m. This derived height accuracy is somewhat less than the error estimated in Section *2.2.1*. The empirical error in Section *2.2.1* is potentially a more comprehensive representation of the DEM total uncertainty, as it encapsulates multiple error sources. While the perpendicular baseline effect on height accuracy is undeniable, it might not always be the dominant error source, especially in the presence of other contributing factors as previously discussed (See Section *2.2.1*).

Table 1: Summary of system attributes and quality metrics for the TanDEM-X dataset under study. The columns, from left to right, indicate the data acquisition date, the central radar incidence angle (θ), the heading angle (α), the perpendicular baseline ($B_\perp$), and the ambiguity height (h_{amb}) for each utilized reference DEM. Dates marked with stars denote the reference TDX DEM acquisition dates from Delgado et al. [2019].

TDX date	θ [deg]	α [deg]	$B_\perp$ [m]	h_{amb} [m]
2011-01-27*	46	−106	−380	−42
2011-03-01	45	−106	−355	−43
2011-08-29*	34	−105	−230	−45
2011-10-07	45	−106	263	58
2011-12-23*	46	−106	169	96
2012-01-08	34	−105	163	64
2012-03-09*	46	−106	−118	−137
2012-03-25*	33	−105	−129	−81
2013-01-11	47	−106	266	62
2013-02-13	45	−106	213	73
2013-09-03	36	−255	180	64
2013-11-08	34	−255	149	71
2013-12-22	35	−255	−158	−69
2014-04-05	47	−254	−146	−113
2014-08-06	46	−106	179	90
2014-08-17	45	−106	179	85
2016-01-10	31	−105	243	40
2016-01-14	48	−254	−50	−341
2016-01-20	35	−255	−109	−101
2016-01-21	32	−105	−243	−41
2019-04-16	47	−254	380	43
2019-11-28	35	−255	−248	−44

To gain deeper insights into the extent and location of areas with high errors or artifacts derived from the side-looking nature of radar imaging systems, we analyzed areas where pronounced topographical variations could lead to phenomena such as foreshortening, layover, or shadow effects [Bamler and Hartl 1998]. In Figure 7, we illustrate the correlation between terrain slope and standard deviation errors within the region of interest. Both the average slope and cumulative local standard deviation are computed within a box of 10 by 10 pixels (75 by 75 meters). To do this, we first calculated the slope and standard deviation for each CoSSC, TDX, and Pléiades DEM separately. Then, we averaged these values over the entire time series, creating a composite estimate of the slope and standard deviation for each pixel in the 10 by 10 box. This process was carried out for each 10 by 10 pixel box in the region of interest, yielding the average slope and standard deviation values depicted in Figure 7. In particular, regions with steep slopes (Figure 7A) and high standard deviations (Figure 7B) are primarily located northeast of the vent, a zone characterized by its significant relief. Other error-prone areas of significance are highlighted in Figure 7 and Figure 13, where individual features are marked by steep slopes and high local standard deviations. On the other hand, areas characterized by relatively low slopes (Figure 7A) and low standard deviations (Figure 7B) appear to be exempt from these topographical effects.

2.2.3 *Volume uncertainties estimation*

To gauge the uncertainty in our volcanic volume change calculations derived from the new CoSSC DEM differences, we adopted the empirical method detailed by Poland [2014]. Specifically, we assessed the volume changes in arbitrary areas within the PCC graben, where we anticipated no surface deformation, and that had similar surface characteristics to the 2011–2012 eruption area. We pinpointed three distinct areas measuring 1 km^2, 4 km^2 (approximating the maximum laccolith extent), and 8 km^2 (approximating the maximum lava flow spread) to conduct our analyses (See Figure 1).

For each of these areas, volume differences across four distinct time periods, which align with our primary volume calculations, were evaluated (Figure 8). The reason for selecting these specific four time frames—27 Jan 2011 to 29 Aug 2011, 29 Aug 2011 to 23 Dec 2011, 23 Dec 2011 to 25 Mar 2012, and 25 Mar 2012 to 12 Apr 2014—was primarily their distinctiveness in showing high changes in the laccolith and lava flow, making these changes easily noticeable. The derived average volume uncertainties for the specified areas are as follows: 0.002 km^3 for the 8 km^2 region, 0.0002 km^3 for the 4 km^2 region, and 0.0001 km^3 for the 1 km^2 region (Figure 8). Correspondingly, the volume-to-area ratio results are 0.0003 km, 0.000 07 km, and 0.0001 km. Notably, these values are several orders of magnitude smaller than the calculated volume changes in both the laccolith and lava flow, so the topographic change uncertainty is negligible for the scope of the study.

2.3 Locating River channels in the DEMs

Our DEMS show elevation chagnes in the river channels over time due to tephra erosion and deposition. Our primary objective in this section is to use the high-precision DEMs to track the changes in locations of the river channels over time, focusing on the elevation changes due to tephra deposition and erosion. Modern advancements in GIS and remote sensing offer powerful capabilities for delineating watersheds and conducting morphometric analysis of drainage basins. The `QGIS 3.30` software was employed on the high-resolution (5m) reference TDX DEMs [Kubanek 2017; Delgado et al. 2019] and Plèiades DEM [Castro et al. 2016; Delgado et al. 2019] to map the stream and catchment area. Initial preprocessing involved the removal of sinks or depressions within the catchment area that might obstruct water flow. We utilized the "fill sinks" algorithm [Wang and Liu 2006] in the `QGIS` System for Automated Geoscientific Analysis (`SAGA`) toolbox for this purpose. Upon

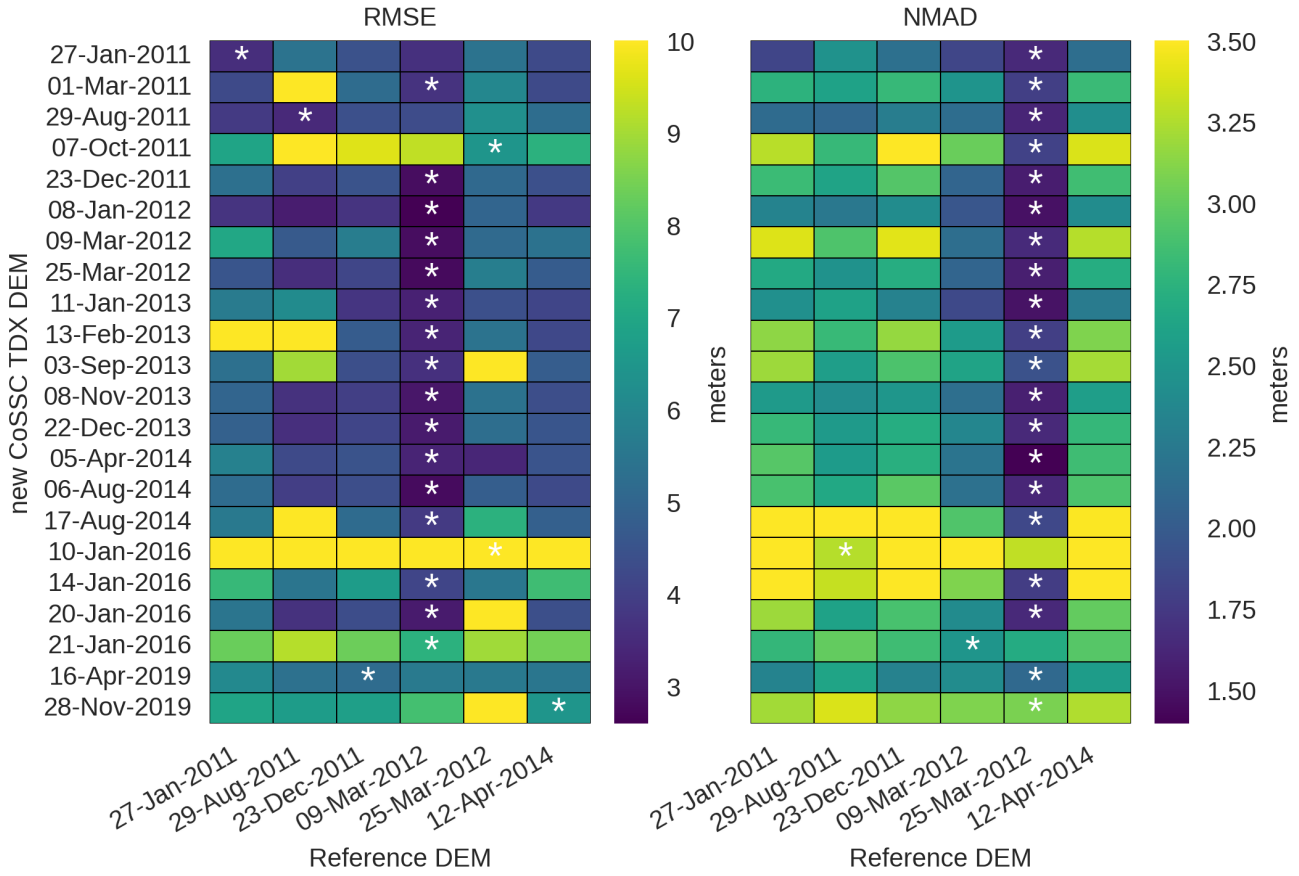

Figure 6: RMSE and NMAD for new CoSSC DEMs compared to the reference (CoSSC and Pléiades) DEMs after masking out the eruption area described by Castro et al. [2016] and Delgado [2021]. The heatmap on the left illustrates the RMSE, with each box representing the RMSE value between a pair of DEMs generated on the corresponding new CoSSC DEMs and the reference TDX DEMs. The heatmap on the right demonstrates the NMAD, following the same structure as the RMSE heatmap. For each row, representing a new CoSSC DEM, the white asterisk marks the new CoSSC DEM that produced the smallest RMSE and NMAD, respectively. Lower values (darker shades) indicate higher match between the new and reference DEMs.

treating the DEMs, we then computed the Strahler stream order using the SAGA toolbox in QGIS. The Strahler methodology starts from the smallest upstream channels and assigns increasing order numbers at confluences where streams of the same order meet. While the computation produced 11 distinct orders, iterative refinement was employed to determine the optimal order value that best represents the actual channel network. However, due to inconsistencies in satellite DEMs—where some might represent upstream channels and others might not—variations in the Strahler order and catchment area values occurred. Given these variations, our primary goal was to identify channels rather than a deep morphological study. We subsequently extracted the longitudinal elevation profiles of each channel over different time points, as illustrated in Figure 14 and Figure 15.

2.4 Fieldwork observations

To complement our remote sensing and analytical approaches, fieldwork was carried out in the Cordón Caulle 2011–2012 eruption area from March 14 to March 25, 2022 to observe tephra deposits and other surface features in and around the laccolith. High-resolution photos (Figure 16) of key geological features were captured during the expedition. These photos, in particular, allowed for an estimation of the height of channels by referencing the height of individuals present in the images. It is important to note, however, that these estimates carry an approximate error of ±2 m due to the inherent limitations of such guesstimations. One of our primary observational focuses was on tephra thickness. We closely inspected areas where tephra layers exhibited signs of erosional processes and thicknesses. These observations allowed for a comparative analysis with DEM time series measurements regarding elevation shifts.

3 Results

3.1 Laccolith evolution: emplacement and post-emplacement

Our analysis of the differential DEMs (dDEMs) revealed a marked topographic elevation increase of approximately 250 m to the immediate east of both the lava flow and the eruptive vent, as shown in Figure 9. This elevation has been

previously noted by Castro et al. [2016], who interpreted and modeled the surface uplift as a consequence of a laccolith intrusion. Such an intrusion is believed to occur at very shallow depths, ranging between 20 and 200 m beneath the surface [Castro et al. 2016]. Furthermore, Delgado et al. [2019] used dDEMs to show a logarithmic trend in the time-series volume data corresponding to both the lava flow and the laccolith intrusion throughout the course of the eruption.

The laccolith-induced displacement was significant enough to be directly observed in the coregistered amplitude images of ENVISAT and TerraSAR-X data used to study the timing of laccolith growth (Figure 2 in Castro et al. [2016]; Figure 6 in Delgado [2021]). This observation suggests that the intrusion began within the first four days of the eruption or approximately a week before the lava flow effusion began [Castro et al. 2016; Delgado 2021].

We calculated linear vertical velocity rates to the dDEMs by fitting a 1st-degree polynomial to the topographic change of a 500 × 500 m area in the central part of the laccolith (the intersection between the two dashed lines in Figure 3) to study the laccolith emplacement and post-emplacement, allowing us to differentiate three distinct periods, as shown in Figure 10.

The three periods we defined correspond to different eruptive and post-eruptive phases and the available (limited) timing of DEMs:

1) The first phase includes both the explosive and first few months of the effusive phase since the first available DEM (August 29, 2011) includes both. The eruption began with an explosive phase from June 4, 2011, with intense seismicity [Wendt et al. 2017; Basualto et al. 2023], reaching its peak with

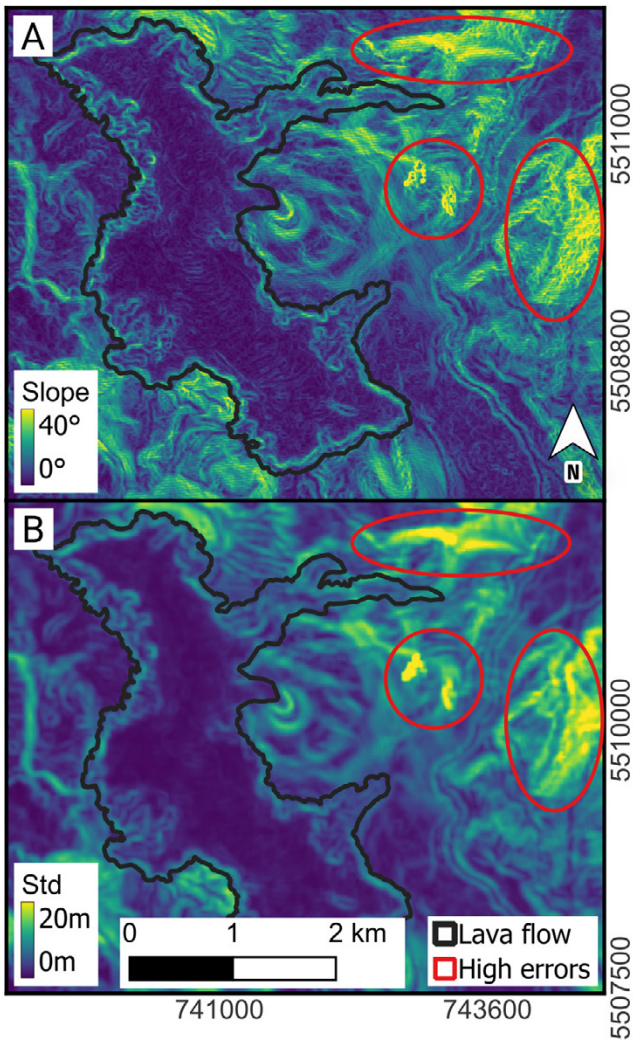

Figure 7: Topographic and error distribution analysis of the area of interest. [A] Shows the mean slope, which was computed using the average slope values from each DEM in the time series within a 10 by 10 pixel (75 by 75 meters) box, highlighting the regional topographic variations. [B] Displays the cumulative standard deviation computed over the entire DEM time series within the same 10 by 10 pixel area. This standard deviation integrates variability from both actual elevation changes and potential errors. The dark outline represents the 2011–2012 lava flow, and areas affected by artifacts are highlighted with red circles.

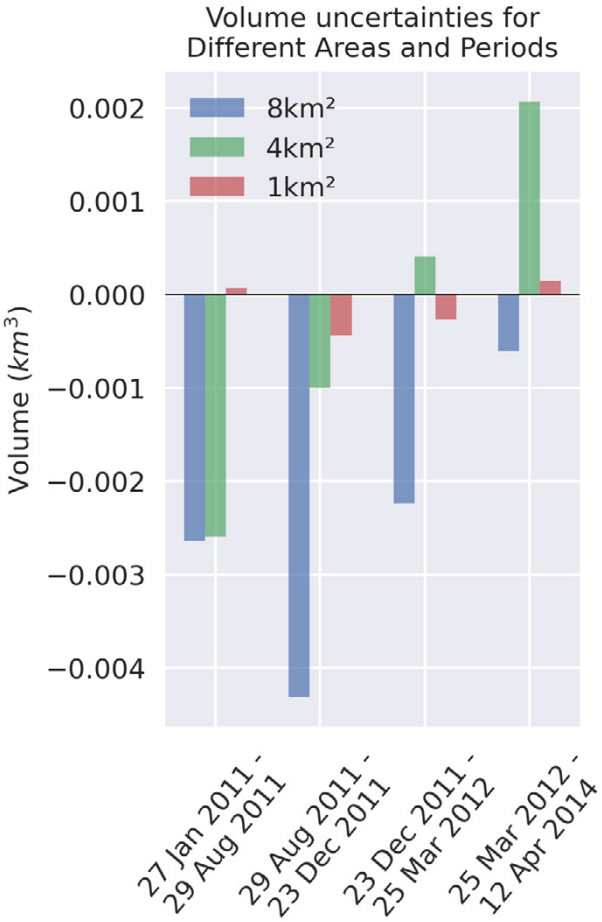

Figure 8: Bar chart representing the volume uncertainties derived from the CoSSC DEM difference for three distinct areas (1 km^2, 4 km^2 and 8 km^2) over four time intervals. The areas correspond to regions within the PCC graben where we anticipated no surface deformation, mirroring the characteristics of the 2011–2012 eruption area (See Figure 1 for location). The y-axis indicates the net volume change in km^3, while the x-axis delineates the time periods.

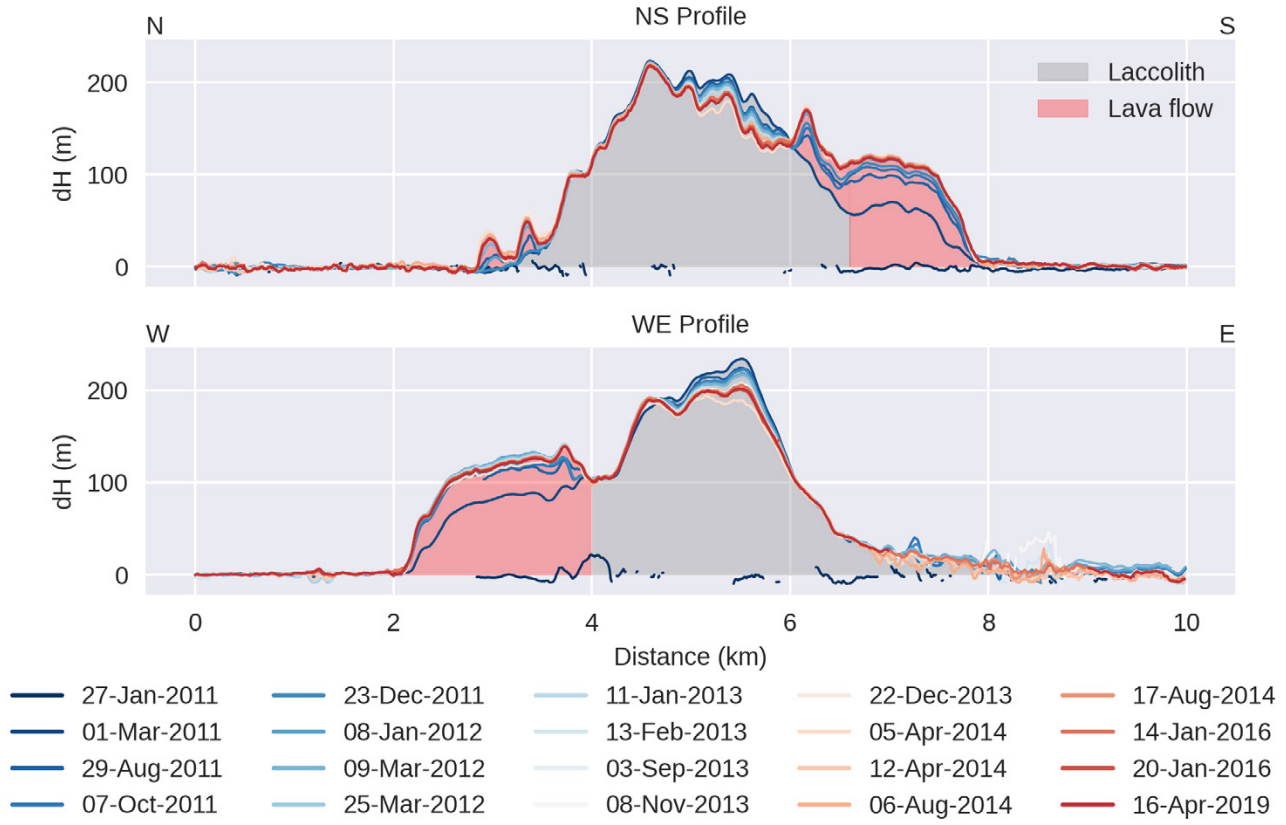

Figure 9: Topographic difference profiles derived from the difference between each post-eruptive DEM and the pre-eruptive DEM (January 27, 2011), illustrating the topographic evolution of the laccolith and lava flow. Profile locations are depicted in Figure 3. The top profile shows the West-East topographic changes for every DEM, and the bottom profile displays the North-South topographic change along with the DEM dates. When interpreting these profiles, it is essential to consider the associated uncertainties: the average NMAD error is 1.8 m and the average RMSE error is 4.3 m (see Section *2.2.1*).

a Plinian VEI 4–5 explosive eruption and a new vent opening near the northeastern branch of Cordón Caulle graben with the LOFZ [Novoa et al. 2022; Basualto et al. 2023]. This first explosive phase concluded on June 14, 2011. Subsequently, an effusive phase was identified, starting on June 15, as indicated by a quasi-harmonic tremor [Bertin et al. 2015]. TSX imagery confirmed a lava flow on June 17, with further validation on June 20 by an overflight, once the eruptive column had subsided [Schipper et al. 2013; Bertin et al. 2015; Basualto et al. 2023]. This effusive phase persisted for months, with intermittent explosive episodes. Notably, a laccolith formed at shallow depths beneath the eruptive vent during this period [Castro et al. 2016]. The total intrusion volume was approximately $1.2\,km^3$ DRE [Delgado et al. 2019]. Concurrently, seismic activities between June and November 2011 at Cordón Caulle's northern branch indicated magma feeding into the growing laccolith [Basualto et al. 2023]. From our CoSSC DEM data, we observed significant uplift by August 9, 2011. The time series from Figure 10 show an average uplift rate of $410\,m\,yr^{-1}$ from January 27 to August 28, 2011, over a $0.25\,km^2$ area. Although there is no obvious difference between the pre-eruptive benchmark (January 27) and the March 1 and August 29 elevation profiles in Figure 9, the lack of good coherence in the TDX DEM on March 1, 2011, limits our ability to calculate the vertical uplift from the start of the eruption on June 4. Consequently, the uplift rate could have been higher if the time period considered was shorter, capturing the initial rapid growth of the laccolith. Deposition of tephra also occurred during this time period (discussed below).

2) The second phase is dominated by continued lava extrusion and laccolith subsidence up to $-12\,m\,yr^{-1}$ between August 29, 2011, and March 25, 2012.

3) The final phase includes lava flow and laccolith subsidence as well as some erosion of tephra in channels (see below). There is a data gap between March 2012 and January 11, 2013, after which we observed an apparently steady laccolith subsidence rate of up to $-0.3\,m\,yr^{-1}$ until November 27, 2019, the date of the last DEM.

We used the dDEMS to calculate the maximum surface subsidence-to-uplift ratio from January 27, 2011 to November 27, 2019 Figure 11. Surface uplift was measured from January 27, 2011 to August 28, 2011, with the subsequent surface subsidence period measured from August 28, 2011 to November 27, 2019. Unlike the velocity rates, this ratio shows the total topographic change, revealing a heterogeneous pattern. The areas with the highest ratios, nearing 20 %, experienced significantly more subsidence compared to uplift, indicating a marked influence of different geological processes in different

areas. Interestingly, outside the area that displays the maximum elevation changes (>50 m) on the laccolith, the highest surface subsidence-to-uplift ratio coincide with the channels or rivers to the southeast of the laccolith within tephra deposition zones from the isopachs and the southeast-directed plume (Figure 11). This observation suggests a spatial correlation between the surface subsidence-to-uplift ratio and these geological features, potentially reflecting their role in shaping the topographic evolution.

Moreover, volume calculations were performed for four dH maps (Figure 12). The results show an initial laccolith volume of 0.455 km^3 for the period ending in August 2011. Following this peak, the laccolith experienced a volume loss of 0.012 km^3 between August 2011 and December 2011. Subsequently, the volume showed a minor increase, registering gains of 0.0071 km^3 and 0.0006 km^3 for the periods ending in March 2012 and April 2014, respectively. However, these gains were more than offset by significant volume losses: 0.015 km^3 between December 2011 and March 2012, and 0.023 km^3 between March 2012 and April 2014. When considering volume uncertainties: for the laccolith area (3.2–3.9 km^2), the volume uncertainty is 0.0003 km^3, indicating that observed volume changes exceed this value, and are therefore significant.

3.2 Lava flows

The lava flows were active between July 15, 2011 and April 2012, both covering new parts of the surface and internally inflating (Figure 3 and Figure 9). Our DEM time series along with Tuffen et al. [2013] and Castro et al. [2016], confirm that the thickness of the lava flow averaged 30 m in the external regions of the flow, and increased to an average of 60 m in the interior sections. It is worth noting that the thickness values reported by Delgado [2021] (>100 m), differ from our measurements. This discrepancy is because their calculations are based on topography prior to the eruption and include both the laccolith uplift and the lava flow. In contrast, our assessments are based on the post-eruptive topography (after the laccolith emplacement). The peak height of the lava flow within the time series was reached on March 9, 2012, during the eruption. In this period, lava discharge rates consistently fluctuated within a range of 10 to 30 $m^3\ s^{-1}$ [Bertin et al. 2015; Coppola et al. 2017], suggesting a relatively stable output during this phase. As outlined by Tuffen et al. [2013], a lava flow with a thickness of 35 m would require over three years to solidify fully. This extended solidification period allows the lava flow to continue supplying its margins, facilitating the flow progression and the formation of break out lobes even after the eruption has ceased [Farquharson et al. 2015]. This stage concluded with a resurgence and intensification of volcanic activity between October 2011 and January 2012. This escalation is characterized by several processes: an increase in the amplitude of the quasi-harmonic tremor [Basualto et al. 2023], the emergence of new ash emissions [Schipper et al. 2013], explosions and lava effusion [Bertin et al. 2015], and a rise in the time-averaged lava discharge rate [Coppola et al. 2017].

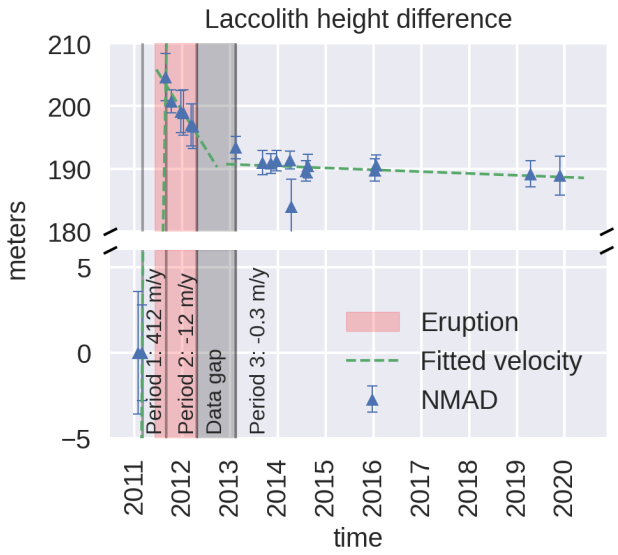

Figure 10: The laccolith average height change (dH) calculated with respect to the January 27, 2011 DEM, over a 500 × 500 m area located at the intersection of the dark lines in Figure 3, subfigures 3A, 3D, and 3G. The NMAD of the new CoSSC DEMs relative to the reference DEM is displayed as error bars. The NMAD calculations were computed outside the eruption area from the studies of Castro et al. [2016] and Delgado [2021]. For each time period, we fit a line to the elevations (green dashed line) and display the slope value (in m yr^{-1}) on the plot.

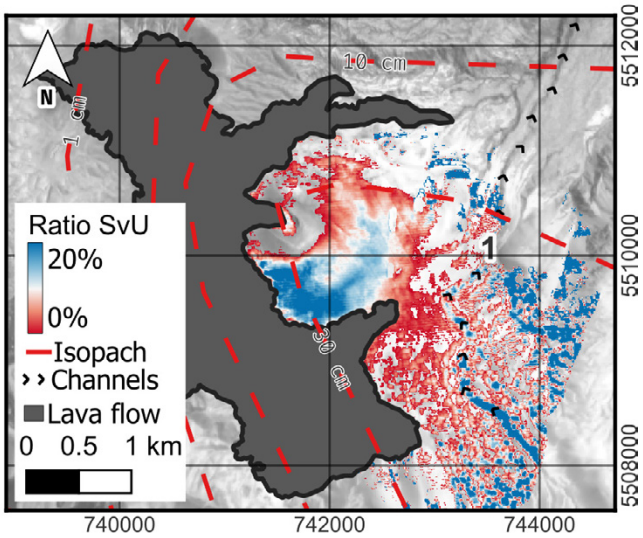

Figure 11: Spatial distribution of surface subsidence-to-uplift ratio occurring between January 27, 2011, and November 27, 2019. Surface uplift was measured from January 27, 2011, to August 28, 2011, with the subsequent surface subsidence period measured from August 28, 2011, to November 27, 2019. The ratio is represented as a percentage of the maximum observed value. The extent of the 2011 lava flow is represented by the grey overlay, while the thin dark lines mark the flow direction of Channel 1 referenced in Figure 13. A potential spatial correlation between the channel and the observed high ratio values is notable.

Additionally, we carried out volume calculations based on four dH maps specific to the lava flow. These results showed an initial volume of 0.326 km^3 for the period ending in August 2011. This was followed by an additional volume gain of 0.184 km^3 from August 2011 to December 2011. The volume continued to increase substantially, adding 0.269 km^3 by the end of March 2012, bringing the total volume to 0.78 km^3—larger than that reported by Coppola et al. [2017]. However, the last period until April 2014 showed a significantly smaller gain of 0.017 km^3. Regarding volume losses, the lava flow showed negligible losses across all periods, with the most significant loss being 0.026 km^3 between March 2012 and April 2014. It is important to highlight the volume uncertainty for the area approximating the lava flow (6.3–7.7 km^2), which is 0.002 km^3. This indicates that while some of the observed volume changes might appear substantial, they are within the error bounds, and their significance needs careful consideration. Overall, the lava flow predominantly experienced volume gains with only minor volume reductions throughout the period up to 2014. However, subsidence is observed on some parts of the lava in 2011 (Figure 13), with more widespread subsidence evident on all parts of the lava in the later period (Figure 3).

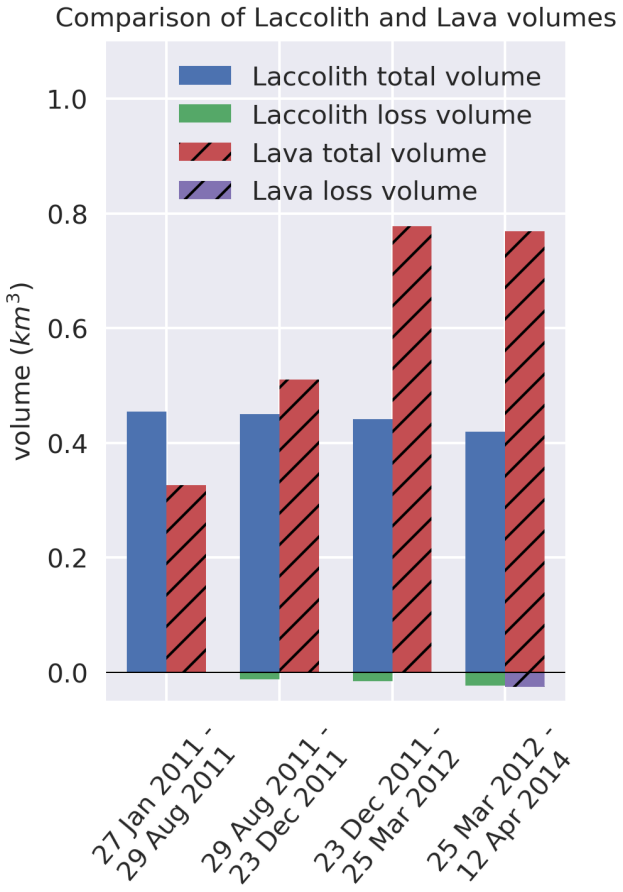

Figure 12: Comparative Volumes of the Laccolith and Lava Flows over time. The bar graph shows the cumulative volume gains (positive values) and losses (negative values) of the laccolith and lava flows for different time periods between 2011 and 2014. The x-axis represents the different periods, formatted as "Start Date - End Date". The y-axis represents the volume in cubic kilometers (km^3). Bars filled with diagonal lines represent lava volumes, while solid bars represent the laccolith volumes.

3.3 Tephra deposition and erosion

We observed distinct elevation changes exceeding 5 m—above the noise threshold for smooth terrain—in the region southeast of the eruptive vent (Figure 13). These changes extend to the boundaries of the TDX and CoSSC DEMs, and lie more than 3 km from the assumed edge of the laccolith (Figure 13). Contrary to the conclusions by Castro et al. [2016], who suggest these elevation increases are due to laccolith deformation, our field observations and subsequent analyses lead us to think the elevation changes are due to tephra deposition and localized erosion.

Isopach diagrams [Bertrand et al. 2014] suggest a maximum tephra thickness of less than 1 m in this area (Figure 1). Nonetheless, field reports and our observations confirm tephra fall deposits within the laccolith area ranging between 5 and 10 m in thickness. Outside this area, deposits exceed 10 m. Our field observations lead us to conclude that elevation gains (<10 m) over a distance of about 5 km to the southeast of the vent are not solely attributable to subsurface magma movements but possibly due to these thicker tephra deposits. Our assessment is consistent with laccolith growth models (see Figure 4 in Castro et al. [2016]) but diverges from previous interpretation in attributing these elevation changes to the southeast of the vent primarily to tephra deposition.

Further support for the interpretation of tephra deposition to the southeast of the vent comes from significant changes in elevation (>10 m) in river channels recorded between January 2011 and April 2014 (Figure 14, Figure 15, and Figure 13). Our March 2022 field photos provide additional visual evidence for this (Figure 16). In channel #1, for example, the TDX data show a an elevation increase of 14–16 m between January 27, 2011 and August 29, 2011 in two locations (Figure 2) where our field observations show about 14–16 m of tephra (Figure 16) falling within theoretical error margins of the DEMs, previously discussed in Section 2.

Noteworthy as well is the significant ratio of surface subsidence to uplift (SvU) in channel #1, as indicated in Figure 11. The temporal evolution of the topography of channel #1 (becoming both deeper and wider) due to channel erosion between 2011 and 2014 are well-documented through the dH values derived from CoSSC DEMs (Figure 13). In most places, the 2014 river channel surface elevations have returned to or are still above their 2011 levels (Figure 15). Interestingly, a few instances were observed where the original channel was incised below the 2011 elevation downstream due to an upstream elevation increase caused by both laccolith and tephra deposition (Figure 14). As an example, channel #1 received up to 50 m of material deposits by August 2011, most of which eroded, leading to a net elevation change of 10 m by April 2014 (Figure 14). Similar dynamics are evident for Channels #2 and #3, as showcased in profiles (c) and (d) of Figure 15.

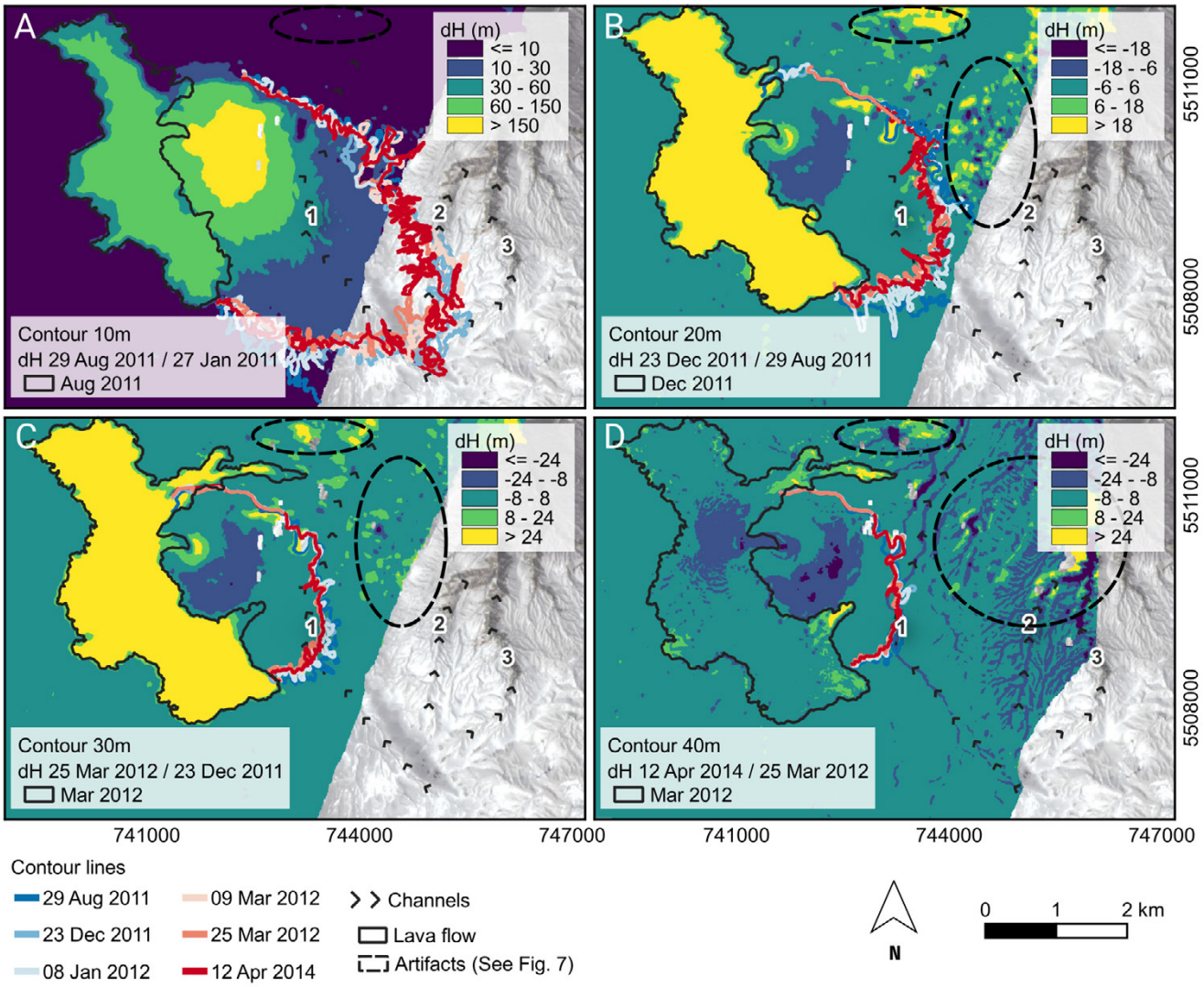

Figure 13: Height difference (dH) color maps of the PCC volcanic complex showing topographical changes between different dates. Arrows over channels indicate the channels downstream (longitudinal profiles found in Figure 14). Thin black lines outline the lava flow at different dates. The colored contour lines show dH between the respective date in the legend and 27 Jan 2011 for the laccolith. [A] displays the 10 m dH contour, and dH map between 29 Aug 2011 and 27 Jan 2011. [B] highlights the 20 m dH contour and dH map between 23 Dec 2011 and 29 Aug 2011. [C] features the 30 m dH contour, and dH map between 25 Mar 2012 and 23 Dec 2011. [D] presents the 40 m dH contour and the dH map between 12 Apr 2014 and 25 Mar 2012.

We have further investigated the size of the laccolith as compared to the area of significant tephra deposition in Figure 13. We approximate the shape of the laccolith as an ellipse [Castro et al. 2016] that best fits each contour of elevation change (dH) for different dates derived from the CoSSC and Plèiades DEMs. The approach of using elliptical fits provides a compact and convenient representation for summarizing the evolving contour shapes, while also offering an effective method to distinguish between short-term terrain changes, which are prone to erosion over time, and more permanent deformations likely associated with laccolith emplacement. Our hypothesis is that the ellipse that approximates the laccolith should not change size over time while an ellipse that includes tephra could change as tephra erodes. For clarification, the aspect ratio in this study is defined as the minor axis divided by the major axis. The 10 m dH contour area experienced an approximate 40 % change between August 2011 and April 2014, while the 20 m contour underwent a 30 % change within the same period. On the other hand, the 30 m and 40 m contours showed minimal changes, with no more than a 1.5 % difference in area. An increasing aspect ratio over time for all contours, as depicted in Figure 17, suggests progressive erosion or material removal. This trend towards a more circular shape from the initial ellipsoidal form provides valuable insights into the rate of surface erosion. These findings underline the rapid transformations in the landscape following a volcanic event, emphasizing that more susceptible areas undergo significant alterations within a few years.

4 Discussion

4.1 Laccolith and lava flow post-emplacement subsidence

Although previous studies have described the uplift mechanism of the laccolith [Castro et al. 2016; Delgado et al. 2019], subsidence of both the laccolith and lava flow remains less discussed, except for a brief mention in Delgado [2021]. Our results provide the first comprehensive analysis of subsidence, revealing both spatial and temporal variability as seen in Figure 3 and Figure 10. Notably, we observed height changes exceeding 50 m and rates over 12 m yr^{-1}, magnitudes previously undocumented in new volcanic deposits with satellite datasets, to our knowledge.

The surface subsidence could be caused by a combination of several different processes that are occurring within the

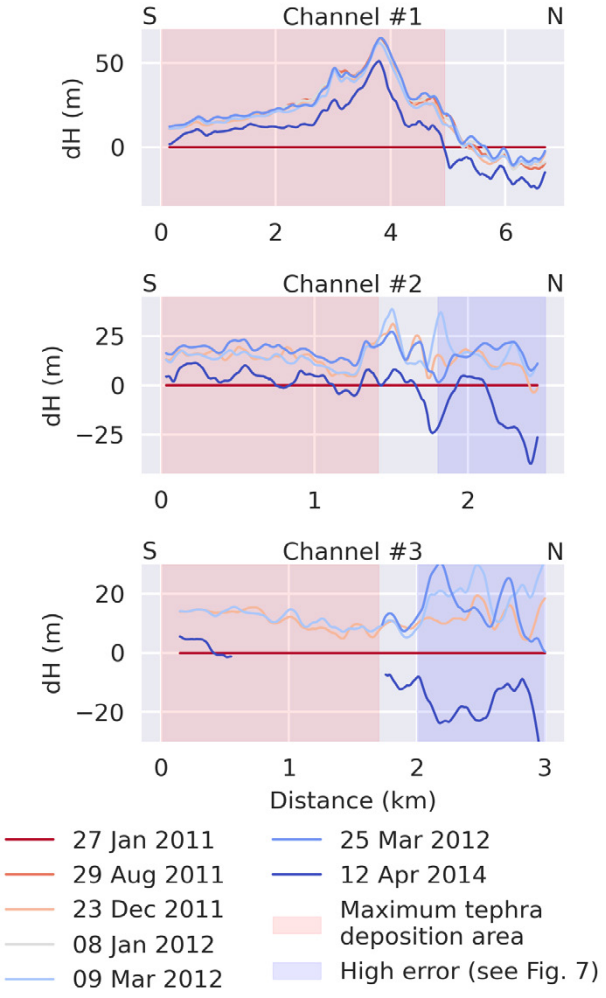

Figure 14: Elevation change (dH) profiles along the channels numbered in Figure 2. The color lines depict the difference in elevation between the specified date and January 27, 2011 (before the eruption). The approximate orientation of each channel is provided at the top of its respective subplot. The red area represents the area of tephra deposition and the blue area shows the area correlated with steep slopes and high errors (See Figure 7).

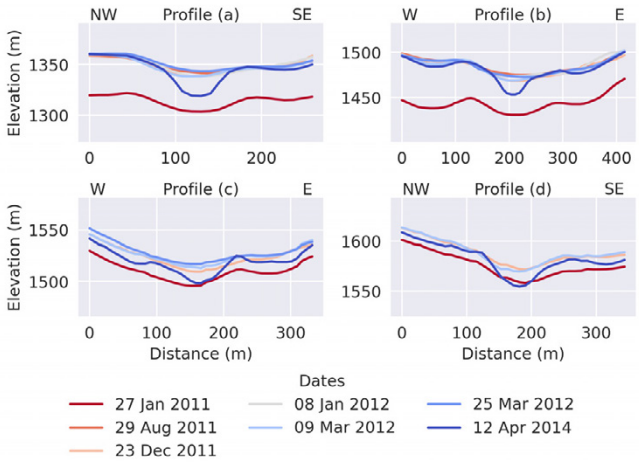

Figure 15: Horizontal profiles for the channels labeled in Figure 2 on the dates shown by each color. The approximate orientation of each horizontal profile is specified at the top of the corresponding subplot.

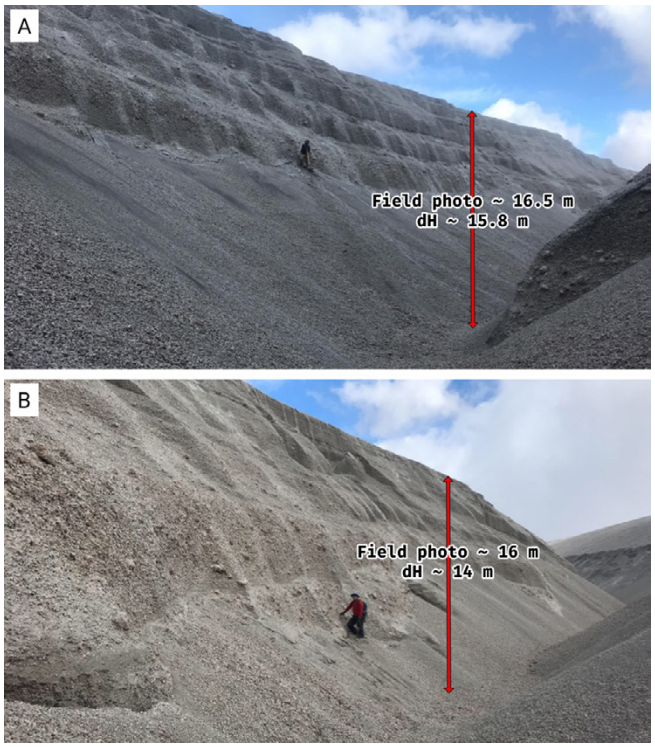

Figure 16: Tephra deposits in channel #1 (locations shown by stars in Figure 2). Photo [A]: Inner section of channel #1 displaying a depth of approximately 16.5 m from the top to the bottom of the ravine in March, 2022. DEM difference between April 2014 and August 2011 at the same location indicates a dH of 15.8 m. Photo [B]: Inner section of channel #1 with an approximate depth of 16 m in March, 2022. DEM change at this location between April 2014 and August 2011 is 14 m. The difference in elevation measured by the dDEMs is less than that measured in the field which could be due in part to additional deepening of the channel between April 2014 and March 2022.

laccolith and the tephra fall deposits upon it: mobilization of partially molten rock, degassing, collapse of pore space, erosion/removal of material, compaction driven by solidification of the laccolith or cooling of the deposits. We do not think that solidification and cooling alone can be driving these high rates of subsidence (up to 30 % of the initial volume) based on the following order of magnitude calculation: the maximum volume change from solidification is 10 % [Fialko et al. 2001] and from complete cooling (from say 1000 to 0 °C, given a coefficient of thermal expansion of $10 \times 10^{-5}\,°C^{-1}$) is only 1 %. Moreover, the solidification and cooling will take decades to centuries, and therefore cannot be driving the high rates observed over the first few years following the eruption. The timescale of thermoelastic contraction is contingent on factors such as the volume and depth of the source, and the thermal diffusivity of the encompassing crust [Furuya 2005]. Evidence from recent investigation made for at Usu volcano in Japan by Wang and Aoki [2019] suggests that a surface subsidence of less than $1\,mm\,yr^{-1}$ would take over 160 years to manifest, given the hypothetical conditions of a heat source with a volume of $5 \times 10^6\,m^3$ situated around 100 m deep, with a temperature of 1000 K, and thermal diffusivity of $1 \times 10^{-5}\,m^2\,s^{-1}$.

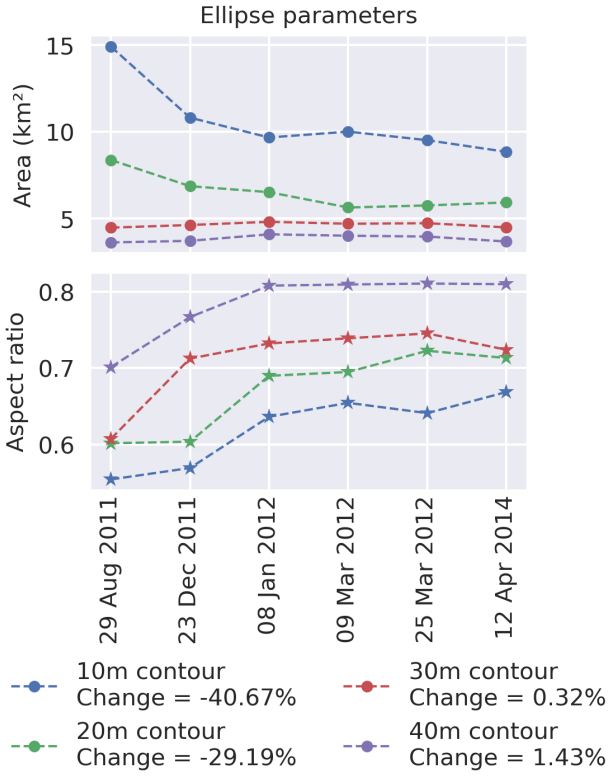

Figure 17: Evolution of best-fitting ellipsoid properties over time for different contours presented in Figure 13. The top panel shows the change in ellipsoidal area (in km^2), while the bottom panel illustrates variations in the aspect ratio, defined here as the minor axis divided by the major axis. Different curves correspond to distinct contour levels. The legend specifies the percentage change in ellipsoid area between August 2011 and April 2014 for each colored contour.

On the other hand, the lava flows show maximum subsidence rates of 1.2–1.4 $m\,yr^{-1}$ in the radar Line-of-sight [Delgado et al. 2016] that, while higher than observed before at lava flows, could be explained by cooling and solidification of the thick flows immediately after deposition [Wang and Aoki 2019].

We propose that several processes contribute to the post-eruptive subsidence observed. These include degassing, draining of a fraction of the laccolith to feed the lava flows, erosion/removal of material, fault relaxation, and collapse of pore space, especially within the tephra deposits on top of the laccolith. Another possibility to consider, as discussed by Wadsworth et al. [2022], is sintering. It is important to note that the area surrounding the laccolith is characterized by an intense fault and fracture array, as observed in the field and in high-resolution satellite imagery [Castro et al. 2016; Magee 2024]. These structural features may have played a significant role in both the syn- and post-emplacement deformation of the laccolith and the overburden. In addition to the compaction and erosion of tephra deposits, the relaxation of faults and fractures could potentially accommodate some of the observed subsidence. The presence of these extensional features, such as graben-like structures, suggests that the local stress field and the mechanical properties of the host rock may have influenced the deformation pattern. A detailed analysis of emplacement and faulting is beyond the scope of this work. It requires the integration of additional field observations to link deformation styles with topography features.

With the data in hand, it is difficult to evaluate the relative role of erosion/removal of material vs. the vertical movement of material that stays in place and undergoes volume change from degassing, draining, and collapse of pore space—but there are additional datasets that could be brought to bear in future studies. Field observations of the extent of tephra erosion will be key. Another tool is InSAR coherence. InSAR signals will be decorrelated on surfaces that undergo significant erosion, but could maintain coherence on surfaces that retain their radar scattering properties, but move vertically. Delgado [2021] noted that InSAR coherence on the laccolith was possible over several weeks to months during the austral summer in 2013, 2014, and 2016 (times restricted to when data were available); because the signal was coherent, erosion/mass removal was probably not significant during those times. Further work using InSAR is needed during other time periods to determine if the absence/presence of InSAR coherence and surface subsidence can be constrained. Updated DEMs for the time periods of the InSAR studies will be needed to ensure that topographic errors from the rapidly subsiding laccolith do not give spurious subsidence signals.

An interesting observation from our study is the comparison between the volume gain in the lava flow and the volume loss in the laccolith during different periods (Figure 12). There is one order of magnitude difference in what the lava flow gained ($0.5\,km^3$) compared to what the laccolith lost ($0.05\,km^3$) in terms of volume between August 2011 and April 2014. Furthermore, during the eruption, the difference was a bit larger, with the lava flow gaining $0.18\,km^3$ while the laccolith lost only $0.01\,km^3$ between August 2011 and December 2011. This disparity suggests that while the laccolith is losing

a minimal volume—possibly through draining into the lava flow along with other mentioned processes—the lava flow is experiencing a significant increase in volume, likely due to deeper magma supply. Given these observations, it is plausible to infer that the supply of magma from the laccolith to the lava flow after emplacement is negligible. This relationship between the lava flow and the laccolith presents an intriguing area for future research, particularly in the modeling of interconnected subterranean magma chambers and lava flow paths.

A striking and unusual feature observed in our study is the non-proportional relationship between the amount of subsidence and the amount of uplift (Figure 11). Despite the north side of the laccolith exhibiting a similar thickness, there is pronounced subsidence on the south side (Figure 9). This distinctive asymmetry in subsidence suggests lateral variability within the laccolith. However, the most compelling insight arises from the correlation with the tephra deposits. Given the robust evidence that the tephra deposits are notably thicker to the southeast of the eruptive vent (see Section 3.3), we advance a nuanced hypothesis: a significant portion of the height change observed, particularly the pronounced asymmetry in subsidence on the laccolith, is likely influenced by post-emplacement processes within the tephra, such as higher surface subsidence or erosion/removal of material. Furthermore, the prospect of the emplaced laccolith primarily feeding the lava flow appears unlikely. This revelation underscores the importance of understanding tephra dynamics post-emplacement and challenges traditional paradigms.

4.2 Comparison to other systems

Instances of shallow-level intrusions, otherwise referred to as laccolith or cryptodome formations, which result in surface uplift are rare in modern times. Only a handful of documented examples exist: notably, the eruption of Showa-shinzan, Usu Volcano, Hokkaido, Japan from 1943–1945 [Minakami et al. 1951; Katsui et al. 1985]; the eruption of Bezymianny, Kamchatka, Russia in 1956 [Belousov 1996]; the 1980 eruption of Mount St. Helens, Washington, USA [Lipman et al. 1981]; and the 2000 eruption of the Nishiyama-Shinzan cryptodome in Usu Volcano. These case studies provide important references for understanding and interpreting the geophysical changes associated with such phenomena.

The Showa-Shinzan cryptodome was formed during the 1943–1945 eruption at Usu volcano [Minakami et al. 1951; Katsui et al. 1985; Yokoyama and Seino 2000; Yokoyama 2002; 2004]. One of the best-documented examples of cryptodome formation, largely due to the "Mimatsu diagram" [Minakami et al. 1951]. Over two years, the formation had four stages: intense seismicity, magma migration, explosions, and dome formation. The emplacement began with dacitic magma intrusion and resultant high-intensity earthquakes on December 28, 1943. Ground uplift began in February 1944, leading to upward bulging and radial surface cracks. Uplift rates ranged from 70 to 550 m yr^{-1} until June 1944. Concurrently, a phreatic eruption occurred from June to October 1944. A final uplift surge and lava dome formation started in December 1945 [Yokoyama 2002; Tanaka et al. 2007], peaking at 219 m yr^{-1} and ending in September 1945, culminated in the formation of the 250–300 m high cryptodome [Minakami et al. 1951; Yokoyama 2004; Goto and Tomiya 2019] with a 100 m lava dome on top [Yokoyama 2002; Tanaka et al. 2007]. Post-eruption, the dome has been continuously subsiding. Notably, it subsided at a rate of around 0.054 m yr^{-1} from 1964 to 1976, and at a slower rate of 0.032 m yr^{-1} from 1976 to 1992 [Yokoyama and Seino 2000]. This trend of subsidence has been corroborated by recent space geodetic observations, which report an ongoing rate of approximately 0.03 m yr^{-1} for the last 25 years [Aoyama et al. 2009; Wang and Aoki 2019]. Furthermore, the dome continues to retain heat from its formation, as the heat has not been completely dissipated. Indeed, the fumarole temperature was recorded at 190 °C in 1997, a decrease from 1000 °C in 1945 and around 500 °C in 1960 [Minakami et al. 1951; Yokoyama and Seino 2000]. Based on these observations, Wang and Aoki [2019] proposed that the observed subsidence can be attributed to the thermal contraction of the cryptodome that has emerged.

The Nishiyama-Shinzan cryptodome formation in 2000 at Usu volcano [Ui et al. 2002; Yamagishi et al. 2004; Saba et al. 2007; Sakagami, M. et al. 2010; Wang and Aoki 2019] is another example of post-emplacement cryptodome. Ground deformation patterns at the site of the 2000 eruption have varied over time. The observations from June 2006 to March 2011 revealed two localized areas of subsidence, one widespread around the NC crater, and a more localized one around the KC crater. This pattern is similar to the coeruptive deformation field and suggests two separate deformation sources under these craters. The differences in the observed deformation area between ascending and descending measurements are interpreted as resulting from the differing looking geometries of the two satellite orbits. Meanwhile, no significant displacements were detected from October 2014 to August 2017, indicating a rapid decay of post-eruptive deformation. The maximum subsidence rates measured from June 2006 to March 2011 and October 2014 to August 2017 were 0.038 m yr^{-1} and 0.006 m yr^{-1} respectively, reinforcing the evidence of a diminishing rate of deformation over time.

The observed high rates of tephra erosion (>15 m yr^{-1}) from the channel southeast of Cordón Caulle correspond with those seen in other fresh volcanic deposits worldwide. For instance, post-eruption at Mount St. Helens, the debris-avalanche deposit underwent significant channel development [Meyer and Martinson 1989]. The 1980 eruption of Mount St. Helens triggered dramatic landscape changes, including substantial erosion predominantly initiated by overland flow and rill erosion, especially on steep slopes. These processes resulted in rapid channel incision and widening immediately post-eruption. Over subsequent years, however, the dominant erosional processes shifted towards more diffusive phenomena such as rainsplash, frost action, and bioturbation. Within 12 years, erosion rates had decreased to levels below the threshold of measurement detection, even on unvegetated surfaces [Collins and Dunne 2019].

Similarly, following the June 1991 eruption at Mount Pinatubo in the Philippines, 6 km^3 of easily erodible pyroclastic-flow material dramatically altered the landscape,

leading to the occurrence of numerous lahars and elevated sediment yields in certain basins. The initial erosion was primarily driven by selective transport of finer-grained sediment and pumice. Over time, as channels incised into valley bottom sediments, gravel-size clasts began to interact and progressive armoring ensued. This process was significantly influenced by the volume and nature of local sediment sources [Gran and Montgomery 2005].

At El Chichón, México, valleys buried in pyroclastic density current (PDC) deposits from the 1982 eruption experienced a swift response, with incision up to 20 m within eight years. Remarkably, most of this incision occurred within the first few months following the eruption [Inbar et al. 2001]. This swift landscape modification underscored high-magnitude accelerated erosion, mainly during the initial year post-eruption. By 1999, the 1 km diameter crater and the 8 km long pyroclastic flows covering the volcano slopes had undergone substantial revegetation. The post-eruption crater lake is continuously being filled by rockfall, landslides, and sediment supply from the crater drainage basin, a process expedited by intense rainfall and chemical precipitation from hot springs at the lake's bottom [Inbar et al. 2001].

These examples demonstrate a common transition pattern in landscapes recovering from major disturbances such as volcanic eruptions. The shift from rapid, flow-driven erosion to slower, diffusive processes reflects an interplay between environmental factors, including weather conditions, vegetation cover, and the physical properties of the erupted material.

5 Conclusion

The analysis of surface elevation changes during and after the 2011–2012 Cordón Caulle rhyolitic eruption has delivered unprecedented insights into the spatiotemporal evolution of laccolith and lava flow emplacement, surface subsidence, and erosional processes in a volcanic environment. Our study underscores the indispensable role of high-resolution topographic data, uniquely offered by the TanDEM-X satellite mission. Without the capabilities of TanDEM-X, such detailed monitoring would be unfeasible, especially as optical missions like Pléiades lack background acquisition programs with the requisite high temporal resolution. This dataset has been instrumental in shedding light on the intricate dynamics of volcanic activity. The satellite-derived insights become particularly crucial when identifying rapid and inconsistent surface subsidence rates, which are often elusive to InSAR due to coherence loss during extensive surface alterations. Additionally, our methodology's inclusion of field observations serves not only as a robust validation mechanism for the satellite data but also enriches our grasp of post-eruptive processes, ensuring a holistic understanding of the phenomenon.

The observed asymmetry in surface subsidence across the laccolith (Figure 10), the substantial thickness of tephra deposits (Figure 13), and the identification of channel tephra erosion (Figure 16) have all highlighted the potential role of both internal and external processes in shaping the post-eruptive landscape. From internal processes such as magma movements, degassing, collapse of pore space, and solidification, to external ones like erosion and removal of material, a multiplicity of factors influence the morphological evolution of a volcanic system following an eruption.

Furthermore, the comparative analysis with other systems worldwide (Section 4), including Mount St. Helens, USA, Mount Pinatubo, Philippines, and El Chichón, México, underscores the universality of rapid post-eruptive topographic changes and points towards shared processes across diverse volcanic systems.

The insights gained from this study offer valuable groundwork for future research aimed at understanding the complexities of magma transport, storage, and post-emplacement subsidence in laccoliths and shallow magma bodies. A key avenue for future work involves developing computational models to better understand the post-eruptive processes within the laccolith, its interaction with the lava flow, and the resulting deformation of the overburden. These models could integrate the high-resolution topographic data and field measurements, thereby providing a more accurate and comprehensive framework for understanding subsidence dynamics and related hazards. This would also pave the way for targeted experimental designs that can provide further validation or refinement of the models. The integration of multi-source data remains crucial for improving the accuracy and reliability of hazard assessments. Future studies should focus on incorporating different monitoring methods, such as gravity and seismicity studies, to build a more holistic understanding of the post-eruptive landscape. This multi-disciplinary approach is key to advancing our current monitoring techniques and developing more effective strategies for risk mitigation. As technological advancements continue to improve our analytical capabilities, we anticipate refining these methods further, advancing to a more comprehensive, and practically applicable, understanding of volcanic dynamics.

Author Contributions

Diego Lobos-Lillo - Data analysis and interpretation, Drafting the article; Mattheu Pritchard - Data analysis and interpretation, Drafting the article; Francisco Delgado - Data collection, Critical revision of the article; Philipp Ruprecht - Data collection, Critical revision of the article; Carolina Muñoz-Saez - Critical revision of the article.

Acknowledgements

This work was partly funded by the National Science Foundation under proposals EAR-1824160 and EAR-2317730. D.L.L. was supported by a Becas Chile fellowship. We extend our gratitude to Joel Scheingross from the University of Nevada, Reno, as well as Joshua Wiejaczka and Thomas Giachetti from the University of Oregon for their critical review, invaluable discussions, and ideas. Likewise, we appreciate Heather Winslow from the University of Nevada-Reno, Patrick Phelps, and Helge Gonnermann from Rice University for their insightful discussions. The Pléiades data are copyright property of Airbus DS, were provided through the CNES ISIS program under an academic license for the research project 16-0219-01-011-114 and are not available for open distribution. TerraSAR-X CoSSCs were provided by Deutsches Zentrum für Luft- und Raum- fahrt (DLR) and Airbus through the Committee

on Earth Observation Satellites Volcano Demonstrator Project and NASA Commercial Smallsat Data Acquisition program augmentation of NASA Science Mission Directorate project 80NSSC21K0842.

Data Availability

All new CoSSC DEM data supporting the findings of this study have been deposited in the Zenodo repository and are freely accessible at the following link: https://zenodo.org/doi/10.5281/zenodo.10045172. This repository pertains specifically to the new CoSSC DEM data used in our research.

Copyright Notice

References

Acocella, V. (2021). *Volcano-Tectonic Processes*. Advances in Volcanology. Cham: Springer International Publishing. ISBN: 978-3-030-65967-7. DOI: 10.1007/978-3-030-65968-4.

Albino, F., B. Smets, N. D'Oreye, and F. Kervyn (2015). "High-resolution TanDEM-X DEM: An accurate method to estimate lava flow volumes at Nyamulagira Volcano (D. R. Congo)". *Journal of Geophysical Research: Solid Earth* 120(6), pages 4189–4207. DOI: 10.1002/2015JB011988.

Aoyama, H., S. Onizawa, T. Kobayashi, T. Tameguri, T. Hashimoto, H. Oshima, and H. Y. Mori (2009). "Inter-eruptive volcanism at Usu volcano: Micro-earthquakes and dome subsidence". *Journal of Volcanology and Geothermal Research* 187(3-4), pages 203–217. DOI: 10.1016/J.JVOLGEORES.2009.09.009.

Bachmann, M., J. H. Gonzalez, G. Krieger, M. Schwerdt, J. W. Antony, and F. De Zan (2012). "Calibration of the bistatic TanDEM-X interferometer". *Proceedings of the European Conference on Synthetic Aperture Radar, EUSAR*. Volume 2012-April, pages 97–100. ISBN: 9783800734047.

Bamler, R. and P. Hartl (1998). "Synthetic aperture radar interferometry". *Inverse Problems* 14(4), R1. DOI: 10.1088/0266-5611/14/4/001.

Barrientos, S. E. (1994). "Large thrust earthquakes and volcanic eruptions". *Pure and Applied Geophysics PAGEOPH* 142(1), pages 225–237. DOI: 10.1007/BF00875972/METRICS.

Basualto, D., A. Tassara, J. Lazo-Gil, L. Franco-Marin, C. Cardona, J. San Martín, F. Gil-Cruz, M. Calabi-Floddy, and C. Farías (2023). "Anatomy of a high-silica eruption as observed by a local seismic network: The June 2011 Puyehue-Cordón Caulle event (southern Andes, Chile)". *Solid Earth* 14(1), pages 69–87. DOI: 10.5194/se-14-69-2023.

Bato, M. G., J. L. Froger, A. J. Harris, and N. Villeneuve (2016). "Monitoring an effusive eruption at Piton de la Fournaise using radar and thermal infrared remote sensing data: Insights into the October 2010 eruption and its lava flows". *Geological Society Special Publication* 426(1), pages 533–552. DOI: 10.1144/SP426.30.

Belousov, A. (1996). "Deposits of the 30 March 1956 directed blast at Bezymianny volcano, Kamchatka, Russia". *Bulletin of Volcanology* 57(8), pages 649–662. DOI: 10.1007/s004450050118.

Bertin, D., L. E. Lara, D. Basualto, A. Amigo, C. Cardona, L. Franco, F. Gil, and J. Lazo (2015). "High effusion rates of the Cordõn Caulle 2011-2012 eruption (Southern Andes) and their relation with the quasi-harmonic tremor". *Geophysical Research Letters* 42(17), pages 7054–7063. DOI: 10.1002/2015GL064624.

Bertrand, S., R. Daga, R. Bedert, and K. Fontijn (2014). "Deposition of the 2011-2012 Cordõn Caulle tephra (Chile, 40S) in lake sediments: Implications for tephrochronology and volcanology". *Journal of Geophysical Research: Earth Surface* 119(12), pages 2555–2573. DOI: 10.1002/2014JF003321.

Bonadonna, C., M. Pistolesi, R. Cioni, W. Degruyter, M. Elissondo, and V. Baumann (2015). "Dynamics of wind-affected volcanic plumes: The example of the 2011 Cordón Caulle eruption, Chile". *Journal of Geophysical Research: Solid Earth* 120(4), pages 2242–2261. DOI: 10.1002/2014JB011478.

Burgmann, R., P. A. Rosen, and E. J. Fielding (2000). "Synthetic aperture radar interferometry to measure earth's surface topography and its deformation". *Annual Review of Earth and Planetary Sciences* 28, pages 169–209. DOI: 10.1146/annurev.earth.28.1.169.

Carlino, S. (2012). "The process of resurgence for Ischia Island (southern Italy) since 55 ka: The laccolith model and implications for eruption forecasting". *Bulletin of Volcanology* 74(5), pages 947–961. DOI: 10.1007/S00445-012-0578-0/FIGURES/9.

Castro, J. M., B. Cordonnier, C. I. Schipper, H. Tuffen, T. S. Baumann, and Y. Feisel (2016). "Rapid laccolith intrusion driven by explosive volcanic eruption". *Nature Communications* 7, pages 1–7. DOI: 10.1038/ncomms13585.

Castro, J. M., C. I. Schipper, S. P. Mueller, A. S. Militzer, A. Amigo, C. S. Parejas, and D. Jacob (2013). "Storage and eruption of near-liquidus rhyolite magma at Cordón Caulle, Chile". *Bulletin of Volcanology* 75(4), pages 1–17. DOI: 10.1007/s00445-013-0702-9.

Chen, C. W. and H. A. Zebker (2000). "Network approaches to two-dimensional phase unwrapping: intractability and two new algorithms". *Journal of the Optical Society of America A* 17(3), page 401. DOI: 10.1364/JOSAA.17.000401.

Collins, B. D. and T. Dunne (2019). "Thirty years of tephra erosion following the 1980 eruption of Mount St. Helens". *Earth Surface Processes and Landforms* 44(14), pages 2780–2793. DOI: 10.1002/esp.4707.

Coppola, D., M. Laiolo, A. Franchi, F. Massimetti, C. Cigolini, and L. E. Lara (2017). "Measuring effusion rates of obsidian lava flows by means of satellite thermal data". *Journal of Volcanology and Geothermal Research* 347, pages 82–90. DOI: 10.1016/j.jvolgeores.2017.09.003.

Corry, C. E. (1988). "Laccoliths; Mechanics of emplacement and growth". *Special Paper of the Geological Society of America* 220, pages 1–116. DOI: 10.1130/SPE220-p1.

Covello, F., F. Battazza, A. Coletta, E. Lopinto, C. Fiorentino, L. Pietranera, G. Valentini, and S. Zoffoli (2010). "COSMO-SkyMed an existing opportunity for observing the Earth". *Journal of Geodynamics* 49(3-4), pages 171–180. DOI: 10.1016/j.jog.2010.01.001.

Craig, H., T. Wilson, C. Stewart, V. Outes, G. Villarosa, and P. Baxter (2016a). "Impacts to agriculture and critical infrastructure in Argentina after ashfall from the 2011 eruption of the Cordón Caulle volcanic complex: An assessment of published damage and function thresholds". *Journal of Applied Volcanology* 5(1), pages 1–31. DOI: 10.1186/S13617-016-0046-1/FIGURES/19.

Craig, H., T. Wilson, C. Stewart, G. Villarosa, V. Outes, S. Cronin, and S. Jenkins (2016b). "Agricultural impact assessment and management after three widespread tephra falls in Patagonia, South America". *Natural Hazards* 82(2), pages 1167–1229. DOI: 10.1007/S11069-016-2240-1/METRICS.

Crozier, J., S. Tramontano, P. Forte, S. J. C. Oliva, H. M. Gonnermann, E. Lev, M. Manga, M. Myers, E. Rader, P. Ruprecht, H. Tuffen, R. Paisley, B. F. Houghton, T. Shea, C. I. Schipper, and J. M. Castro (2022). "Outgassing through magmatic fractures enables effusive eruption of silicic magma". *Journal of Volcanology and Geothermal Research* 430, page 107617. DOI: 10.1016/J.JVOLGEORES.2022.107617.

Delgado, F. (2021). "Rhyolitic volcano dynamics in the Southern Andes: Contributions from 17 years of InSAR observations at Cordón Caulle volcano from 2003 to 2020". *Journal of South American Earth Sciences* 106, page 102841. DOI: 10.1016/j.jsames.2020.102841.

Delgado, F., J. Kubanek, K. Anderson, P. Lundgren, and M. Pritchard (2019). "Physicochemical models of effusive rhyolitic eruptions constrained with InSAR and DEM data: A case study of the 2011-2012 Cordón Caulle eruption". *Earth and Planetary Science Letters* 524. DOI: 10.1016/j.epsl.2019.115736.

Delgado, F., M. E. Pritchard, D. Basualto, J. Lazo, L. Córdova, and L. E. Lara (2016). "Rapid reinflation following the 2011–2012 rhyodacite eruption at Cordón Caulle volcano (Southern Andes) imaged by InSAR: Evidence for magma reservoir refill". *Geophysical Research Letters* 43(18), pages 9552–9562. DOI: 10.1002/2016GL070066.

Delgado, F., M. E. Pritchard, S. Samsonov, and L. Córdova (2018). "Renewed Posteruptive Uplift Following the 2011–2012 Rhyolitic Eruption of Cordón Caulle (Southern Andes, Chile): Evidence for Transient Episodes of Magma Reservoir Recharge During 2012–2018". *Journal of Geophysical Research: Solid Earth* 123(11), pages 9407–9429. DOI: 10.1029/2018JB016240.

Dominguez, L., C. Bonadonna, P. Forte, P. A. Jarvis, R. Cioni, L. Mingari, D. Bran, and J. E. Panebianco (2020). "Aeolian Remobilisation of the 2011-Cordón Caulle Tephra-Fallout Deposit: Example of an Important Process in the Life Cycle of Volcanic Ash". *Frontiers in Earth Science* 7, page 486343. DOI: 10.3389/FEART.2019.00343/BIBTEX.

Dominguez, L., C. Bonadonna, C. Frischknecht, S. Menoni, and A. Garcia (2021). "Integrative Post-event Impact Assessment Framework for Volcanic Eruptions: A Disaster Forensic Investigation of the 2011–2012 Eruption of the Cordón Caulle Volcano (Chile)". *Frontiers in Earth Science* 9, page 645945. DOI: 10.3389/FEART.2021.645945/BIBTEX.

Elissondo, M., V. Baumann, C. Bonadonna, M. Pistolesi, R. Cioni, A. Bertagnini, S. Biass, J. C. Herrero, and R. Gonzalez (2016). "Chronology and impact of the 2011 Cordón Caulle eruption, Chile". *Natural Hazards and Earth System Sciences* 16(3), pages 675–704. DOI: 10.5194/NHESS-16-675-2016.

Euillades, P. A., L. D. Euillades, M. H. Blanco, M. L. Velez, P. Grosse, and G. J. Sosa (2017). "Co-eruptive subsidence and post-eruptive uplift associated with the 2011–2012 eruption of Puyehue-Cordón Caulle, Chile, revealed by DInSAR". *Journal of Volcanology and Geothermal Research* 344, pages 257–269. DOI: 10.1016/j.jvolgeores.2017.06.023.

Farquharson, J. I., M. R. James, and H. Tuffen (2015). "Examining rhyolite lava flow dynamics through photo-based 3D reconstructions of the 2011–2012 lava flowfield at Cordón-Caulle, Chile". *Journal of Volcanology and Geothermal Research* 304, pages 336–348. DOI: 10.1016/J.JVOLGEORES.2015.09.004.

Farr, T. G., P. A. Rosen, E. Caro, R. Crippen, R. Duren, S. Hensley, M. Kobrick, M. Paller, E. Rodriguez, L. Roth, D. Seal, S. Shaffer, J. Shimada, J. Umland, M. Werner, M. Oskin, D. Burbank, and D. E. Alsdorf (2007). "The shuttle radar topography mission". *Reviews of Geophysics* 45(2), page 2004. DOI: 10.1029/2005RG000183.

Fialko, Y., M. Simons, and Y. Khazan (2001). "Finite source modelling of magmatic unrest in Socorro, New Mexico, and Long Valley, California". *Geophysical Journal International* 146(1), pages 191–200. DOI: 10.1046/j.1365-246X.2001.00453.x.

Fisher, P. F. and N. J. Tate (2006). "Causes and consequences of error in digital elevation models". *Progress in Physical Geography* 30(4), pages 467–489. DOI: 10.1191/0309133306pp492ra.

Furuya, M. (2005). "Quasi-static thermoelastic deformation in an elastic half-space: theory and application to InSAR observations at Izu-Oshima volcano, Japan". *Geophysical Journal International* 161(1), pages 230–242. DOI: 10.1111/J.1365-246X.2005.02610.X.

Global Volcanism Program (2023). *[Database] Volcanoes of the World (v. 5.1.0; 9 Jun 2023).* Technical report. Global Volcanism Program.

Goldstein, R. M. and C. L. Werner (1998). "Radar interferogram filtering for geophysical applications". *Geophysical Research Letters* 25(21), pages 4035–4038. DOI: 10.1029/1998GL900033.

Goto, Y. and A. Tomiya (2019). "Internal structures and growth style of a quaternary subaerial rhyodacite cryptodome at Ogariyama, Usu Volcano, Hokkaido, Japan". *Frontiers in Earth Science* 7, page 416549. DOI: 10.3389/feart.2019.00066.

Gran, K. B. and D. R. Montgomery (2005). "Spatial and temporal patterns in fluvial recovery following volcanic eruptions: Channel response to basin-wide sediment loading at Mount Pinatubo, Philippines". *Bulletin of the Geological Society of America* 117(1-2), pages 195–211. DOI: 10.1130/B25528.1.

Grémion, S., V. Pinel, T. Shreve, F. Beauducel, R. Putra, A. Solikhin, A. B. Santoso, and H. Humaida (2023). "Tracking the evolution of the summit lava dome of Merapi volcano between 2018 and 2019 using DEMs derived from TanDEM-X and Pléiades data". *Journal of Volcanology and Geothermal Research* 433(December 2022). DOI: 10.1016/j.jvolgeores.2022.107732.

Gudmundsson, A., K. Drymoni, J. Browning, V. Acocella, F. Amelung, F. L. Bonali, A. Elshaafi, I. Galindo, N. Geshi, A. Geyer, M. J. Heap, Ö. Karaoğlu, S. Kusumoto, J. Marti, V. Pinel, A. Tibaldi, T. Thordarson, and T. R. Walter (2022). "Volcanotectonics: the tectonics and physics of volcanoes and their eruption mechanics". *Bulletin of Volcanology* 84(8), pages 1–8. DOI: 10.1007/S00445-022-01582-4/FIGURES/2.

Hanssen, R. F. (2001). *Radar Interferometry: Data Interpretation and Error Analysis*. Kluwer Academic Publishers. ISBN: 0-7923-6945-9.

Höhle, J. and M. Höhle (2009). "Accuracy assessment of digital elevation models by means of robust statistical methods". *ISPRS Journal of Photogrammetry and Remote Sensing* 64(4), pages 398–406. DOI: 10.1016/J.ISPRSJPRS.2009.02.003.

Inbar, M., A. Reyes Enriquez, and J. H. Graniel Graniel (2001). "Morphological changes and erosion processes following the 1982 eruption of El Chichón volcano, Chiapas, Mexico / Modifications géomorphologiques et processus d'érosion consécutifs à l'éruption du volcan El Chichón, Chiapas, Mexico, en 1982". *Géomorphologie relief processus environnement* 7(3), pages 175–183. DOI: 10.3406/morfo.2001.1100.

Jay, J., F. Costa, M. Pritchard, L. Lara, B. Singer, and J. Herrin (2014). "Locating magma reservoirs using InSAR and petrology before and during the 2011-2012 Cordón Caulle silicic eruption". *Earth and Planetary Science Letters* 395, pages 254–266. DOI: 10.1016/j.epsl.2014.03.046.

Katsui, Y., H. Komuro, and T. Uda (1985). "Development of faults and growth of Usu-Shinzan cryptodome in 1977-1982 at Usu Volcano, North Japan". *Journal of the Faculty of Science, Hokkaido University* 21(3), pages 339–362.

Krieger, G., A. Moreira, H. Fiedler, I. Hajnsek, M. Werner, M. Younis, and M. Zink (2007). "TanDEM-X: A satellite formation for high-resolution SAR interferometry". *IEEE Transactions on Geoscience and Remote Sensing* 45(11), pages 3317–3340. DOI: 10.1109/TGRS.2007.900693.

Kubanek, J. (2017). "Volcano monitoring with bistatic TanDEM-X SAR interferometry". PhD thesis. Karlsruher Institut für Technologie (KIT), page 156. ISBN: 978-3-7696-5205-5. DOI: 10.5445/IR/1000065004.

Kubanek, J., M. P. Poland, and J. Biggs (2021). "Applications of bistatic radar to volcano topography-a review of ten years of TanDEM-X". *IEEE Journal of Selected Topics in Applied Earth Observations and Remote Sensing* 14, pages 3282–3302. DOI: 10.1109/JSTARS.2021.3055653.

Lara, L. E., J. A. Naranjo, and H. Moreno (2004). "Rhyodacitic fissure eruption in Southern Andes (Cordón Caulle; 40.5°S) after the 1960 (Mw:9.5) Chilean earthquake: A structural interpretation". *Journal of Volcanology and Geothermal Research* 138(1-2), pages 127–138. DOI: 10.1016/j.jvolgeores.2004.06.009.

Lara, L. E., A. Lavenu, J. Cembrano, and C. Rodríguez (2006). "Structural controls of volcanism in transversal chains: Resheared faults and neotectonics in the Cordón Caulle-Puyehue area (40.5°S), Southern Andes". *Journal of Volcanology and Geothermal Research* 158(1-2), pages 70–86. DOI: 10.1016/j.jvolgeores.2006.04.017.

Lipman, P. W., J. G. Moore, and D. A. Swanson (1981). "Bulging of the north flank before the May 18 Eruption - Geodetic data". *US Geological Survey Professional Paper* 1250, pages 143–155.

Livingstone, C., I. Sikaneta, and C. Gierull (2006). "RADARSAT-2 system and mode description". *Defence Research and Development Canada Ottawa* (2005), pages 1–22.

Magee, C. (2024). "Fractures and faults across intrusion-induced forced folds: a georesource perspective". *Geological Society, London, Special Publications* 547(1). DOI: 10.1144/SP547-2023-47.

Martone, M., B. Bräutigam, P. Rizzoli, C. Gonzalez, M. Bachmann, and G. Krieger (2012). "Coherence evaluation of TanDEM-X interferometric data". *ISPRS Journal of Photogrammetry and Remote Sensing* 73, pages 21–29. DOI: 10.1016/J.ISPRSJPRS.2012.06.006.

Menand, T. (2011). "Physical controls and depth of emplacement of igneous bodies: A review". *Tectonophysics* 500(1-4), pages 11–19. DOI: 10.1016/j.tecto.2009.10.016.

Meyer, D. F. and H. A. Martinson (1989). "Vitesse et processus de développement des chenaux du réseau hydrographique et de son rètablissement après l'éruption de 1980 de Mont Ste Hélène, Washington". *Hydrological Sciences Journal* 34(2), pages 115–127. DOI: 10.1080/02626668909491318.

Minakami, T., T. Ishikawa, and K. Yagi (1951). "The 1944 Eruption of Volcano Usu in Hokkaido, Japan: History and mechanism of formation of the new dome "Syowa-Sinzan"". *Bulletin Volcanologique* 11(1), pages 45–157. DOI: 10.1007/BF02596029.

Naranjo, J. A., B. S. Singer, B. R. Jicha, H. Moreno, and L. E. Lara (2017). "Holocene tephra succession of Puyehue-Cordón Caulle and Antillanca/Casablanca volcanic complexes, southern Andes (40–41°S)". *Journal of Volcanology and Geothermal Research* 332, pages 109–128. DOI: 10.1016/J.JVOLGEORES.2016.11.017.

Novoa, C., M. Gerbault, D. Remy, J. Cembrano, L. E. Lara, J. Ruz-Ginouves, A. Tassara, J. C. Baez, R. Hassani, S. Bonvalot, and R. Contreras-Arratia (2022). "The 2011 Cordón Caulle eruption triggered by slip on the Liquiñe-Ofqui fault system". *Earth and Planetary Science Letters* 583, page 117386. DOI: 10.1016/j.epsl.2022.117386.

Nuth, C. and Kääb (2011). "Co-registration and bias corrections of satellite elevation data sets for quantifying glacier thickness change". *Cryosphere* 5(1), pages 271–290. DOI: 10.5194/tc-5-271-2011.

Phelps, P. R., H. M. Gonnermann, H. Winslow, P. Ruprecht, M. E. Pritchard, F. Delgado, and Y. Liao (2023). "Feasibility of melt segregation from a crystal mush in response to the 2011–2012 eruption at Cordón Caulle, Chile". *Geophysical Journal International* 235(1), pages 610–634. DOI: 10.1093/GJI/GGAD259.

Pistolesi, M., R. Cioni, C. Bonadonna, M. Elissondo, V. Baumann, A. Bertagnini, L. Chiari, R. Gonzales, M. Rosi, and L. Francalanci (2015). "Complex dynamics of small-moderate volcanic events: the example of the 2011 rhyolitic Cordón Caulle eruption, Chile". *Bulletin of Volcanology* 77(1), pages 1–24. DOI: 10.1007/s00445-014-0898-3.

Poland, M. P. (2014). "Time-averaged discharge rate of subaerial lava at Kīlauea Volcano, Hawai'i, measured from TanDEM-X interferometry: Implications for magma supply and storage during 2011-2013". *Journal of Geophysical Research: Solid Earth* 119(7), pages 5464–5481. DOI: 10.1002/2014JB011132.

Poland, M. P. and H. A. Zebker (2022). "Volcano geodesy using InSAR in 2020: the past and next decades". *Bulletin of Volcanology* 84(3), pages 1–8. DOI: 10.1007/s00445-022-01531-1.

Rizzoli, P., M. Martone, C. Gonzalez, C. Wecklich, D. Borla Tridon, B. Bräutigam, M. Bachmann, D. Schulze, T. Fritz, M. Huber, B. Wessel, G. Krieger, M. Zink, and A. Moreira (2017). "Generation and performance assessment of the global TanDEM-X digital elevation model". *ISPRS Journal of Photogrammetry and Remote Sensing* 132, pages 119–139. DOI: 10.1016/J.ISPRSJPRS.2017.08.008.

Rosen, P. A., E. Gurrola, G. F. Sacco, and H. Zebker (2012). "The InSAR scientific computing environment". *Proceedings of the European Conference on Synthetic Aperture Radar, EUSAR* 2012-April, pages 730–733.

Rosenqvist, A., M. Shimada, N. Ito, and M. Watanabe (2007). "ALOS PALSAR: A pathfinder mission for global-scale monitoring of the environment". *IEEE Transactions on Geoscience and Remote Sensing* 45(11), pages 3307–3316. DOI: 10.1109/TGRS.2007.901027.

Saba, M., Y. Nishida, T. Mogi, S. Takakura, and N. Matsushima (2007). "Development of geothermal field following the 2000 eruption of Usu volcano as revealed by ground temperature, resistivity and self-potential variations". *Annals of Geophysics* 50(1), pages 79–92.

Sakagami, M., H. Sasaki, and S. Mukoyama (2010). "Estimation of Ground Movement Caused By the 2000 Eruption of Usu Volcano , From the Geomorphic Image Analysis of Lidar Dems". *Archives* XXXVIII(Figure 1), pages 293–297.

Schipper, C. I., J. M. Castro, B. M. Kennedy, H. Tuffen, J. Whattam, F. B. Wadsworth, R. Paisley, R. H. Fitzgerald, E. Rhodes, L. N. Schaefer, P. A. Ashwell, P. Forte, G. Seropian, and B. V. Alloway (2021). "Silicic conduits as supersized tuffisites: Clastogenic influences on shifting eruption styles at Cordón Caulle volcano (Chile)". *Bulletin of Volcanology* 83(2), pages 1–22. DOI: 10.1007/s00445-020-01432-1.

Schipper, C. I., J. M. Castro, H. Tuffen, M. R. James, and P. How (2013). "Shallow vent architecture during hybrid explosive-effusive activity at Cordón Caulle (Chile, 2011-12): Evidence from direct observations and pyroclast textures". *Journal of Volcanology and Geothermal Research* 262, pages 25–37. DOI: 10.1016/j.jvolgeores.2013.06.005.

Segall, P. (2013). "Volcano deformation and eruption forecasting". *Geological Society Special Publication* 380(1), pages 85–106. DOI: 10.1144/SP380.4/ASSET/665BA60E-300A-4107-AB6D-37F8ADBF0625/ASSETS/IMAGES/LARGE/SP380-302F15.JPG.

Sepúlveda, F., K. Dorsch, A. Lahsen, S. Bender, and C. Palacios (2004). "Chemical and isotopic composition of geothermal discharges from the Puyehue-Cordón Caulle area (40.5°S), Southern Chile". *Geothermics* 33(5), pages 655–673. DOI: 10.1016/j.geothermics.2003.10.005.

Sepúlveda, F., A. Lahsen, S. Bonvalot, J. Cembrano, A. Alvarado, and P. Letelier (2005). "Morpho-structural evolution of the Cordón Caulle geothermal region, Southern Volcanic Zone, Chile: Insights from gravity and 40Ar / 39Ar dating". *Journal of Volcanology and Geothermal Research* 148(1-2), pages 165–189. DOI: 10.1016/J.JVOLGEORES.2005.03.020.

Seropian, G., C. I. Schipper, L. J. Harmon, S. L. Smithies, B. M. Kennedy, J. M. Castro, B. V. Alloway, and P. Forte (2021). "A century of ongoing silicic volcanism at Cordón Caulle, Chile: New constraints on the magmatic system involved in the 1921–1922, 1960 and 2011–2012 eruptions". *Journal of Volcanology and Geothermal Research* 420. DOI: 10.1016/j.jvolgeores.2021.107406.

Singer, B. S., B. R. Jicha, M. A. Harper, J. A. Naranjo, L. E. Lara, and H. Moreno-Roa (2008). "Eruptive history, geochronology, and magmatic evolution of the Puyehue-Cordón Caulle volcanic complex, Chile". *Bulletin of the Geological Society of America* 120(5-6), pages 599–618. DOI: 10.1130/B26276.1.

Stearns, D. W. (1978). "Faulting and forced folding in the Rocky Mountains foreland". *Memoir of the Geological Society of America* 151, pages 1–37. DOI: 10.1130/MEM151-P1.

Tanaka, H. K., T. Nakano, S. Takahashi, J. Yoshida, H. Ohshima, T. Maekawa, H. Watanabe, and K. Niwa (2007). "Imaging the conduit size of the dome with cosmic-ray muons: The structure beneath Showa-Shinzan Lava Dome, Japan". *Geophysical Research Letters* 34(22). DOI: 10.1029/2007GL031389.

Torres, R., P. Snoeij, D. Geudtner, D. Bibby, M. Davidson, E. Attema, P. Potin, B. Ö. Rommen, N. Floury, M. Brown, I. N. Traver, P. Deghaye, B. Duesmann, B. Rosich, N. Miranda, C. Bruno, M. L'Abbate, R. Croci, A. Pietropaolo, M. Huchler, and F. Rostan (2012). "GMES Sentinel-1 mission". *Remote Sensing of Environment* 120, pages 9–24. DOI: 10.1016/j.rse.2011.05.028.

Tuffen, H., M. R. James, J. M. Castro, and C. I. Schipper (2013). "Exceptional mobility of an advancing rhyolitic obsidian flow at Cordón Caulle volcano in Chile". *Nature Communications* 4(1), pages 1–7. DOI: 10.1038/ncomms3709.

Ui, T., M. Nakagawa, C. Inaba, M. Yoshimoto, and J. R. G. f. t. U. 2. e. Geological Party (2002). "Sequence of the 2000 eruption, Usu Volcano". *Bulletic of Volcanological Society Japan* 47(3), pages 105–117. DOI: 10.18940/KAZAN.56.4-5{_}137.

Vergara-Pinto, F. and J. E. Romero (2023). "Percepciones de las erupciones pasadas y futuras del Puyehue-Cordón Caulle (sur de Chile): conectando vecindad, cohesión social y memoria de desastres en la investigación del riesgo volcánico". *Revista de Estudios Latinoamericanos sobre Reducción del Riesgo de Desastres REDER* 7(2), pages 88–110. DOI: 10.55467/reder.v7i2.126.

Wadge, G., P. Cole, A. Stinton, J. C. Komorowski, R. Stewart, A. C. Toombs, and Y. Legendre (2011). "Rapid topographic change measured by high-resolution satellite radar at Soufriere Hills Volcano, Montserrat, 2008-2010". *Journal of Volcanology and Geothermal Research* 199(1-2), pages 142–152. DOI: 10.1016/j.jvolgeores.2010.10.011.

Wadsworth, F. B., E. W. Llewellin, J. M. Castro, H. Tuffen, C. I. Schipper, J. E. Gardner, J. Vasseur, A. Foster, D. E. Damby, I. M. McIntosh, S. Boettcher, H. E. Unwin, M. J. Heap, J. I. Farquharson, D. B. Dingwell, K. Iacovino, R. Paisley, C. Jones, and J. Whattam (2022). "A reappraisal of explosive–effusive silicic eruption dynamics: syn-eruptive assembly of lava from the products of cryptic fragmentation". *Journal of Volcanology and Geothermal Research* 432, page 107672. DOI: 10.1016/J.JVOLGEORES.2022.107672.

Wang, L. and H. Liu (2006). "An efficient method for identifying and filling surface depressions in digital elevation models for hydrologic analysis and modelling". *International Journal of Geographical Information Science* 20(2), pages 193–213. DOI: 10.1080/13658810500433453.

Wang, X. and Y. Aoki (2019). "Posteruptive Thermoelastic Deflation of Intruded Magma in Usu Volcano, Japan, 1992–2017". *Journal of Geophysical Research: Solid Earth* 124(1), pages 335–357. DOI: 10.1029/2018JB016729.

Wendt, A., A. Tassara, J. C. Báez, D. Basualto, L. E. Lara, and F. García (2017). "Possible structural control on the 2011 eruption of Puyehue-Cordón Caulle Volcanic Complex (southern Chile) determined by InSAR, GPS and seismicity". *Geophysical Journal International* 208(1), pages 134–147. DOI: 10.1093/gji/ggw355.

Wilson, T., C. Stewart, H. Bickerton, P. Baxter, A. V. Outes, G. Villarosa, and E. Rovere (2013). "Impacts of the June 2011 Puyehue-Cordón Caulle volcanic complex eruption on urban infrastructure, agriculture and public health". *Institute of Geology and Nucelar Sciences* 2012, pages 1–88.

Winslow, H., P. Ruprecht, H. M. Gonnermann, P. R. Phelps, C. Muñoz-Saez, F. Delgado, M. Pritchard, and A. Amigo (2022). "Insights for crystal mush storage utilizing mafic enclaves from the 2011–12 Cordón Caulle eruption". *Scientific Reports* 12(1), pages 1–14. DOI: 10.1038/s41598-022-13305-y.

Yamagishi, H., T. Watanabe, and F. Yamazaki (2004). "Sequence of faulting and deformation during the 2000 eruptions of the Usu Volcano, Hokkaido, Japan-interpretation and image analyses of aerial photographs". *Geomorphology* 57(3-4), pages 353–365. DOI: 10.1016/S0169-555X(03)00165-X.

Yokoyama, I. (2002). "Growth mechanism of the 1944 lava dome of Usu volcano in Hokkaido, Japan". *Proceedings of the Japan Academy Series B: Physical and Biological Sciences* 78(1), pages 6–11. DOI: 10.2183/pjab.78.6.

– (2004). "Formation processes of the 1909 Tarumai and the 1944 Usu lava domes in Hokkaido, Japan". *Annals of Geophysics* 47(6), pages 1811–1825.

Yokoyama, I. and M. Seino (2000). "Geophysical comparison of the three eruptions in the 20th century of Usu volcano, Japan". *Earth, Planets and Space* 52(2), pages 73–89. DOI: 10.1186/BF03351616.

Yoon, Y. T., M. Eineder, N. Yague-Martinez, and O. Montenbruck (2009). "TerraSAR-X precise trajectory estimation and quality assessment". *IEEE Transactions on Geoscience and Remote Sensing* 47(6), pages 1859–1868. DOI: 10.1109/TGRS.2008.2006983.